

15 Jun 2006

**FINAL TECHNICAL REPORT
ONR GRANT N00014-04-100200**

Title: Near Wall Velocity And Vorticity Measurements,
In A Very High R_θ Turbulent Boundary Layer

Prepared for: Dr. Ronald Joslin, Program Director
Turbulence and Wakes

Prepared by: Mr. Scott. C. Treat
Prof. John F. Foss
Department of Mechanical Engineering
Michigan State University
East Lansing, MI 48824

Abstract:

Velocity and vorticity measurements have been obtained at two y^+ values: 810 and 2,150, in the very high R_θ ($O 10^6$) turbulent boundary layer at the SLTEST site, Dugway Proving Grounds, Utah. Detailed descriptions of the experimental procedures are reported in order to allow the processed results to be evaluated. The research focus is on the velocity-vorticity products that appear in the formal statement of the vertical gradient of the kinematic Reynolds stress. Statistical data for the velocity and vorticity fields are presented. The cospectra for $v\omega_z$ and $w\omega_y$ show the unexpected result that intermediate wave numbers provide the majority of the contributions to these products.

DISTRIBUTION STATEMENT A
Approved for Public Release
Distribution Unlimited

20060630252

REPORT DOCUMENTATION PAGE				Form Approved OMB No. 0704-0188	
<p>The public reporting burden for this collection of information is estimated to average 1 hour per response, including the time for reviewing instructions, searching existing data sources, gathering and maintaining the data needed, and completing and reviewing the collection of information. Send comments regarding this burden estimate or any other aspect of this collection of information, including suggestions for reducing the burden, to Department of Defense, Washington Headquarters Services, Directorate for Information Operations and Reports (0704-0188), 1215 Jefferson Davis Highway, Suite 1204, Arlington, VA 22202-4302. Respondents should be aware that notwithstanding any other provision of law, no person shall be subject to any penalty for failing to comply with a collection of information if it does not display a currently valid OMB control number.</p> <p>PLEASE DO NOT RETURN YOUR FORM TO THE ABOVE ADDRESS.</p>					
1. REPORT DATE (DD-MM-YYYY)		2. REPORT TYPE Final		3. DATES COVERED (From - To) 01-04-2004 - 15-06-2006	
4. TITLE AND SUBTITLE Near Wall Velocity and Vorticity Measurements, in a Very High R(theta) Turbulent Boundary Layer			5a. CONTRACT NUMBER		
			5b. GRANT NUMBER N00014-04-100200		
			5c. PROGRAM ELEMENT NUMBER		
6. AUTHOR(S) Treat, Scott C., and Foss, John F.			5d. PROJECT NUMBER 04PR05548-00		
			5e. TASK NUMBER		
			5f. WORK UNIT NUMBER		
7. PERFORMING ORGANIZATION NAME(S) AND ADDRESS(ES) Michigan State University 301 Administration Building East Lansing, MI 48824			8. PERFORMING ORGANIZATION REPORT NUMBER		
9. SPONSORING/MONITORING AGENCY NAME(S) AND ADDRESS(ES) Office of Naval Research Regional Office Chicago 230 South Dearborn, Room 380 Chicago, IL 60604-1595 Fax: (312) 886-2094			10. SPONSOR/MONITOR'S ACRONYM(S) ONR		
			11. SPONSOR/MONITOR'S REPORT NUMBER(S)		
12. DISTRIBUTION/AVAILABILITY STATEMENT Approved for public release; distribution is unlimited					
13. SUPPLEMENTARY NOTES					
14. ABSTRACT <p>Velocity and vorticity measurements have been obtained at two y^+ values: 810 and 2,150, in the very high $R(\theta)$ (O 106) turbulent boundary layer at the SLTEST site, Dugway Proving Grounds, Utah. Detailed descriptions of the experimental procedures are reported in order to allow the processed results to be evaluated. The research focus is on the velocity-vorticity products that appear in the formal statement of the vertical gradient of the kinematic Reynolds stress. Statistical data for the velocity and vorticity fields are presented. The cospectra for $v(z)$ and $w(y)$ show the unexpected result that intermediate wave numbers provide the majority of the contributions to these products.</p>					
15. SUBJECT TERMS <p>velocity and vorticity measurements, near-wall, very high $R(\theta)$ turbulent boundary layer.</p>					
16. SECURITY CLASSIFICATION OF:			17. LIMITATION OF ABSTRACT UU	18. NUMBER OF PAGES	19a. NAME OF RESPONSIBLE PERSON John F. Foss
a. REPORT	b. ABSTRACT	c. THIS PAGE			19b. TELEPHONE NUMBER (Include area code) 517-355-3337

TABLE OF CONTENTS

TABLE OF CONTENTS.....	I
LIST OF TABLES	IV
LIST OF FIGURES.....	V
NOMENCLATURE	VIII
ABSTRACT.....	XI
1. INTRODUCTION.....	1
1.1 Research Description	1
1.2 The Study of Turbulent Boundary Layers at High Re.....	2
2. BACKGROUND	4
2.1 Mean Momentum Balance	4
2.2 Scaling	5
2.3 Mean Velocity Profile and Surface Roughness	7
2.4 Thermal Stability	8
2.5 Current Understanding	9

3. MEASUREMENT LOCATION FOR THE PRESENT STUDY	10
4. EXPERIMENTAL METHODS	12
4.1 Equipment	12
4.1.1 Data Cart and Measurement Equipment.....	12
4.1.2 MSU Compact Vorticity Probe.....	14
4.1.3 The Pulse-Width Modulated Constant Temperature Anemometer	18
4.2 Thermal Anemometry Techniques.....	19
4.2.1 Hot-wire Calibration	19
4.2.2 Hot-wire Calibration Correction	23
4.2.3 Velocity Processing Algorithm.....	23
4.2.4 Vorticity Processing Algorithm	25
4.3 Surface Shear-Stress Estimate.....	28
4.4 Experimental Procedure	30
5. RESULTS AND DISCUSSION	35
5.1 Daily Specifics.....	37
5.1.1 June 13 th , 2003 ($y^+ = 810$).....	37
5.1.2 June 4 th , 2003 ($y^+ = 2150$, $y^+ = 1850$)	41
5.2 Velocity Measurements	44
5.2.1 Comparison between using local and linear-fit for direction of U	44
5.2.2 Tabulated Statistics	45

5.2.3	Probability Density	47
5.2.4	Spectral Representation	53
5.3	Vorticity and Velocity-Vorticity Statistics.....	57
5.3.1	Tabulated Results.....	57
5.3.2	Probability Density	60
5.3.3	Spectral Representation	66
6.	CONCLUSIONS.....	71
	REFERENCES.....	73

LIST OF TABLES

Table 5-1 Comparison between methods of determining direction of U	44
Table 5-2 Dimensional Velocity Statistics	46
Table 5-3 Inner Normalized Velocity Statistics.....	46
Table 5-4 Kinematic Reynolds Shear Stress Values.....	46
Table 5-5 Vorticity Statistics	59
Table 5-6 Inner Normalized Vorticity Statistics.....	59

LIST OF FIGURES

Figure 3-1 Topology of the SLTEST site	11
Figure 4-1 Photo of Data Cart and Measurement Equipment.....	14
Figure 4-2 Illustration of hot-wire array used on the vorticity probes.....	17
Figure 4-3 Straight-wire separation distance determination.....	17
Figure 4-4 Typical post-calculated calibration data with high external wind speed	22
Figure 4-5 Typical post-calculated calibration data with low external wind speed	22
Figure 4-6 Hot-wires forming the X must agree on speed and angle	24
Figure 4-7 Example of Typical hot-wire calibration, x-wire at $\gamma = 12^\circ$	25
Figure 4-8 Schematic of microcirculation domain	28
Figure 4-9 Velocity profile at SLTEST site [Metzger, University of Utah, 2004].....	30
Figure 4-10 Photo of deployed probes and wind-tracking probe holding assembly.	34
Figure 4-11 Photo of mounted probes, tripod, and windvane.....	34
Figure 5-1 Wind direction with respect to magnetic North. $y^+ = 810$	40
Figure 5-2 Mean wind speed and trend line over collection period at $y^+ = 810$	40
Figure 5-3 Wind direction with respect to magnetic North. $y^+ = 2150$	43
Figure 5-4 Mean wind speed data and trend line over collection period at $y^+ = 2150$	43
Figure 5-5 Joint probability density of u and v at $y^+ = 810$	48
Figure 5-6 Joint probability density of u and v at $y^+ = 1860$	49
Figure 5-7 Joint probability density of u and v at $y^+ = 2150$	49
Figure 5-8 Joint probability density of u and w at $y^+ = 810$	50
Figure 5-9 Joint probability density of u and w at $y^+ = 2150$	50
Figure 5-10 Weighted joint probability density of u and v at $y^+ = 810$	51

Figure 5-11 Weighted joint probability density of u and v at $y^+ = 1860$	51
Figure 5-12 Weighted joint probability density of u and v at $y^+ = 2150$	52
Figure 5-13 Weighted joint probability density of u and w at $y^+ = 810$	52
Figure 5-14 Weighted joint probability density of u and w at $y^+ = 2150$	53
Figure 5-15 Premultiplied velocity autospectra at $y^+ = 810$	55
Figure 5-16 Premultiplied velocity autospectra at $y^+ = 2150$	55
Figure 5-17 Premultiplied u and v cospectrum at $y^+ = 810$	56
Figure 5-18 Premultiplied u and v cospectrum at $y^+ = 1860$	56
Figure 5-19 Premultiplied u and v cospectrum at $y^+ = 2150$	57
Figure 5-20 Joint probability density of v and ω_z at $y^+ = 810$	61
Figure 5-21 Joint probability density of v and ω_z at $y^+ = 1860$	61
Figure 5-22 Joint probability density of v and ω_z at $y^+ = 2150$	62
Figure 5-23 Joint probability density of w and ω_y at $y^+ = 810$	62
Figure 5-24 Joint probability density of w and ω_y at $y^+ = 2150$	63
Figure 5-25 Weighted joint probability density of v and ω_z at $y^+ = 810$	63
Figure 5-26 Weighted joint probability density of v and ω_z at $y^+ = 1860$	64
Figure 5-27 Weighted joint probability density of v and ω_z at $y^+ = 2150$	64
Figure 5-28 Weighted joint probability density of w and ω_y at $y^+ = 810$	65
Figure 5-29 Weighted joint probability density of w and ω_y at $y^+ = 2150$	65
Figure 5-30 Premultiplied ω_z and ω_y autospectra at $y^+ = 810$	67
Figure 5-31 Premultiplied ω_z and ω_y autospectra at $y^+ = 2150$	67
Figure 5-32 Premultiplied v and ω_z cospectrum at $y^+ = 810$	68
Figure 5-33 Premultiplied v and ω_z cospectrum at $y^+ = 1860$	68

Figure 5-34 Premultiplied v and ω_z cospectrum at $y^+ = 2150$	69
Figure 5-35 Premultiplied w and ω_y cospectrum at $y^+ = 810$	69
Figure 5-36 Premultiplied w and ω_y cospectrum at $y^+ = 2150$	70
Figure 5-37 Premultiplied $v\omega_z$ and $w\omega_y$ cospectra at $y^+ = 810$	70
Figure 5-38 Premultiplied $v\omega_z$ and $w\omega_y$ cospectra at $y^+ = 2150$	71

NOMENCLATURE

Arabic

Re	Reynolds Number
Re_θ	Reynolds Number based on momentum deficit thickness, equation 1.1
U_∞	Free stream velocity
y	Wall-normal height
Θ_0	Adiabatic temperature
k	Wavenumber
f	Sampling frequency
Q	Effective velocity magnitude
T	Temperature
$A, B, \text{ and } n$	Constants that must be determined for each hot-wire
t	Time
q	Flow speed
i	Time step index
U	Mean streamwise velocity
k_s	surface roughness length
$-\overline{uv}$	kinematic Reynolds shear stress
y_p	wall-normal height of peak TKE production
Δs	Length along streamlines
u	Fluctuating streamwise velocity component
v	Fluctuating wall-normal velocity component
w	Fluctuating transverse velocity component

\vec{V} Velocity vector

Greek

δ Boundary layer thickness

ρ Fluid density

ε Dissipation rate

λ Taylor microscale length

ϕ Angle

ℓ Monin-Obukov length

ζ Stability parameter

κ von Karman constant

τ Heating pulse-width

$\tau(t)$ Time series obtained at sampling frequency

τ_w Surface shear-stress

ω_z Vorticity component normal to xy-plane

ω_y Vorticity component normal to xz-plane

ν Kinematic viscosity of the fluid

θ Fluctuation in temperature

γ Angle of the oncoming flow with respect to the axis of the probe body

Superscripts

$+$ Variables scaled on inner parameters

$'$ Denotes rms of fluctuating value.

Subscripts

1,2 Specifies hot wire, section 4.2.4

Abbreviations

ASL Atmospheric Surface Layer

TBL Turbulent Boundary Layer

SLTEST Surface Layer and Environmental Science Test

CVP Compact Vorticity Probes

MSU-CVP MSU Compact Vorticity Probe

PWM-CTA Pulse Width Modulated Constant Temperature Anemometer

SWAW Speed wire/angle wire

ABSTRACT

Velocity and vorticity measurements have been obtained at two y^+ values: 810 and 2,150, in the very high $Re(O 10^6)$ turbulent boundary layer at the SLTEST site, Dugway Proving Grounds, Utah. Detailed descriptions of the experimental procedures are reported in order to allow the processed results to be evaluated. The research focus is on the velocity-vorticity products that appear in the formal statement of the vertical gradient of the kinematic Reynolds stress. Statistical data for the velocity and vorticity fields are presented. The cospectra for $v\omega_z$ and $w\omega_y$ show the unexpected result that intermediate wave numbers provide the majority of the contributions to these products.

1. Introduction

1.1 Research Description

The focus of the present research is the measurement of near-wall turbulent flow statistical quantities within a well-developed zero-pressure-gradient turbulent boundary layer (TBL) at Reynolds numbers (Re) on the order of $R_\theta \sim 10^6$, where

$$R_\theta \equiv \frac{U_\infty \theta}{\nu} \quad (0.1)$$

Such flows are of great technological importance; examples of which may be found about the surfaces of airplanes, high-speed trains, and submarines. Detailed measurements of the smallest scales of motion in such high Reynolds number flows impose challenges to conventional laboratory techniques because of the very small scales of the associated motions. As a consequence, there is a relative scarcity of information about these flows (Metzger and Klewicki 2000). The present research overcomes obstacles of scale and resolution by measuring in the naturally occurring atmospheric boundary layer at a remote site in Utah's western desert. Heated-wire thermal anemometry techniques were used to acquire detailed velocity and vorticity measurements in the near-wall region of the atmospheric surface layer. Statistical analyses of these data are presented. The information gained may be useful in the examination of current theoretical work and in validation of turbulence models.

1.2 The Study of Turbulent Boundary Layers at High Re

Many properties of turbulent boundary layer flow have been shown to be Reynolds number (Re) dependent (Metzger and Klewicki 2000; Wei *et al* 2003). Although turbulent boundary layers (TBL) have been well studied, lower Re results cannot be extrapolated to higher Re without a mathematical basis or empirical support. That is, further experimentation is needed to quantify flow properties at very high Re.

There are significant challenges associated with making detailed near-wall turbulence measurements at high Re. These are imposed by size limitations of laboratory facilities and resolution limitations of current probes. Reynolds number is increased by increasing the length scale, increasing velocity, or decreasing viscosity, or a combination of the three.

Increasing wind tunnel size to accommodate the length scale requirements for the present study is both financially and structurally prohibitive (Metzger and Klewicki 2000). Another approach is to manipulate the kinematic viscosity of air with pressure. The Princeton University facility uses this approach, operating at higher than atmospheric pressures (Metzger and Klewicki 2000).

High Reynolds numbers are more commonly achieved through the use of large wind tunnels and relatively high free stream velocity. Unfortunately, for a given facility size, either an increase in velocity or a decrease in viscosity causes a thinning of the boundary layer thickness. Further, as Reynolds numbers increase the smallest scales become smaller relative to the boundary layer thickness. Thus, sensor size becomes a limiting factor in measuring small scales of motion in high Re laboratory flows.

Some notable laboratory facilities involved in high Re research include: the Princeton University “Superpipe”, the National Diagnostic Facility at Illinois Institute of Technology and the National Transonic Facility at NASA Langley (Metzger and Klewicki 2000). To this date the highest Reynolds number for which small scale properties have been measured in a laboratory is $R_\theta = 31000$ (DeGraaff and Eaton 2000).

The Surface Layer and Environmental Science Test (SLTEST) site located on the U. S. Army’s Dugway Proving Ground in Utah’s western desert was established to permit measurement of the atmospheric surface layer (ASL) as it flows over the unique dry basin of ancient Lake Bonneville. Reynolds numbers at the site are typically on the order of $R_\theta \cong 5 \times 10^6$ (Metzger and Klewicki 2000). Surface features and prevailing wind conditions at the site create conditions that closely resemble a canonical turbulent boundary layer as might be produced in a laboratory environment. The length scales associated with the ASL far exceed those of any laboratory and are sufficiently large to permit the measurement of the smallest scales of motion even at these very high Re values. The results of detailed velocity and vorticity measurements of the ASL at the SLTEST site are presented in chapter 5.

The results presented in this report have been added to the results collected by Priyadarshana and Klewicki in the form of a paper that has been accepted by the *Journal of Fluid Mechanics*. See Priyadarshana, et al. (2006).

2. Background

2.1 Mean Momentum Balance

The mean momentum balance for an incompressible, statistically stationary, turbulent boundary layer over a flat plate is expressed as

$$U \frac{\partial U}{\partial x} + V \frac{\partial U}{\partial y} = \frac{\partial}{\partial y} \left(\nu \frac{\partial U}{\partial y} - \overline{uv} \right) \quad (0.2)$$

The vorticity vector (ω) is the curl of the velocity vector.

$$\omega = \nabla \times \vec{V} \quad (0.3)$$

and it is related to the circulation by equation (0.4);

$$\Gamma = \int_c \vec{V} \cdot d\vec{s} = \int \vec{\omega} \cdot \hat{n} dA \quad (0.4)$$

It can be seen through the tensor identity

$$\frac{\partial \overline{u_i u_j}}{\partial x_j} = -\varepsilon_{ijk} \overline{u_j \omega_k} + \frac{1}{2} \frac{\partial \overline{u_i u_j}}{\partial x_i} \quad (0.5)$$

that the gradient of the negative kinematic Reynolds shear stress may be expressed in terms of the velocity-vorticity products as

$$\frac{\partial \overline{uv}}{\partial y} = \overline{w \omega_y} - \overline{v \omega_z} + \frac{\partial (\overline{v^2 + w^2 - u^2})}{\partial x} \quad (0.6)$$

For a well developed turbulent boundary layer it is reasonable to neglect the streamwise gradient and make the approximation

$$\frac{\partial \overline{uv}}{\partial y} \approx \overline{w \omega_y} - \overline{v \omega_z} \quad (0.7)$$

which has been shown to be a suitable approximation over a range of Re by Klewicki (1989). The importance of the gradient in the left hand side of **Error! Reference source not found.** is apparent where it contributes to the mean momentum balance. As a consequence of **Error! Reference source not found.**, the gradient term can be obtained from the velocity-vorticity statistics collected at a single point. Analysis of the velocity-vorticity product may be used to gain insight into features contributing to the gradient of the Reynolds stress.

2.2 Scaling

Scaling parameters are generally divided into inner and outer groupings. The outer scales are appropriate for examining the boundary layer as a whole. The relevant length and velocity scales are the boundary layer thickness (δ) and the free stream velocity (U_∞). Inner scales are used to characterize the near-wall flow. Inner scaling units are formed from the surface shear-stress (τ_w), the fluid density (ρ), and the kinematic viscosity of the fluid (ν). The friction velocity

$$U_\tau \equiv \sqrt{\tau_w / \rho} \quad (0.2)$$

and viscous length scale

$$l^+ = \frac{\nu}{u_\tau} \quad (0.3)$$

are the common inner units. Variables scaled on inner parameters will be assigned the plus superscript ($^+$) as is common practice.

Several types of scaling are used for examining turbulence. The largest features of turbulence are on the order of the boundary layer thickness, so outer scaling may be

used in examining the largest features of turbulence. At the smallest scales, turbulent kinetic energy is dissipated through viscous shearing. Komogorov introduced the concept of a *universal equilibrium* which asserts that regardless of the stirring mechanism, turbulence kinetic energy is dissipated at small scales where the dissipation rate (ε) and ν are the relevant parameters (Bernard and Wallace 2002). From these two parameters the Komogorov length scale

$$\eta \equiv \frac{\nu^{3/4}}{\varepsilon^{1/4}} \quad (0.4)$$

and dissipation time scale

$$t_d = \left(\frac{\nu}{\varepsilon} \right)^{1/2} \quad (0.5)$$

are formed.

The Taylor microscale (or just microscale), λ , is a length scale related to the small motions over which dissipation takes place. It is formed from a Taylor series expansion of the spatial velocity correlation about zero. The first three terms of the Taylor series form a parabolic approximation of the correlation function. The parabolic approximation has a zero-crossing at distance λ . The Taylor microscale has further importance as an estimation of dissipation in homogenous isotropic turbulence through (Bernard and Wallace 2002).

$$\varepsilon = 15\nu \frac{\overline{u^2}}{\lambda_v^2} \quad (0.6)$$

where

$$\overline{v'(t) * v'(t + \tau)} = 1 - \frac{\tau^2}{\lambda_v^2} + \dots \quad (0.7)$$

An important observation regarding length scales is that the ratio of the largest scales of motion (outer scales) to the smallest scales of motion (inner scales) increases with increasing Reynolds number. Clarifying the significance of the separation of scales remains one of the important objectives of current research.

2.3 Mean Velocity Profile and Surface Roughness

The TBL velocity profile over a smooth wall has been well studied. Beyond the viscous sublayer and buffer layer (approximately $y^+ = 30$) the velocity profile closely matches the logarithmic profile:

$$\overline{U^+} = \frac{1}{0.41} \ln y^+ + 5.2 \quad (0.8)$$

The numerical values in (0.8) are supported by many, but not all, turbulent boundary layer studies and they have been shown to be suitable over a wide range of Re (Pope 2000). Far from the wall there is some deviation from the logarithmic profile. As Re increases, the distance from the wall in y^+ increases over which the logarithmic profile fits.

Surface roughness is known to affect the mean velocity profile. The effect of surface roughness is an offset or additive shift. Krogstad *et al* (1992) approximate the offset as

$$\Delta \overline{U^+} = \frac{1}{\kappa} \ln(k_s^+) - 3.2 \quad (0.9)$$

2.4 Thermal Stability

A thermally unstable atmosphere is one in which there is a negative temperature gradient in the wall-normal direction. This negative temperature gradient gives rise to turbulent motions as a result of buoyant forces. Conversely a thermally stable condition tends to damp turbulent motions. The SLTEST site is unstable during the daytime and passes through neutral conditions, near dusk, to a stable condition. The opposite transition: stable to unstable, occurs in the early morning hours.

The stability parameter ζ is calculated at wall-normal height y using the Monin-Obukov length ℓ .

$$\zeta = \frac{y}{\ell} \quad (0.10)$$

where the Monin-Obukov length ℓ is

$$\ell = \frac{\Theta_0 u_\tau^3}{\kappa g \theta v} \quad (0.11)$$

κ is the von Karman constant, Θ_0 the adiabatic temperature, and θ is the fluctuation in temperature. Physically, ℓ represents a measure of the vertical length over which buoyant effects become comparable in magnitude to other sources of turbulence.

Because the temperature gradient in the surface layer changes continually over time with buoyant forces always present to some degree, neutrality must be defined in a relative sense. That is, if buoyant forces can be considered negligible then the atmosphere can be characterized as neutral. In the ASL, ℓ is rarely found to be less than 10m except in periods of extremely light winds (Tennekes and Lumley 1972). Hence, buoyancy is usually negligible in the near-wall region. To further minimize buoyancy effects, data were collected for the present study during the evening period of transition

between an unstable and stable ASL as the near-wall temperature gradient passes through zero.

2.5 Current Understanding

Whereas detailed statistical quantities in turbulent boundary layers at low Reynolds numbers have been documented extensively, similar research at high Reynolds numbers is much more limited. Metzger and Klewicki (2000) were among the first to probe a turbulent boundary layer at high Reynolds numbers ($Re = 5 \times 10^6$). They examined flow in the viscous sublayer and buffer layer to explore the influence of very high Reynolds number. They conclude that many turbulent boundary layer characteristics in these regions are independent of Reynolds number. Scaling turbulent properties is also a topic of discussion. Metzger *et al* (2001) have looked at examination of mixed scaling versus inner scaling alone at very high Re . DeGraaff and Eaton (2000) also explore scaling of the flat-plate turbulent boundary layer.

Of particular relevance to the present work are studies of velocity and vorticity. Extensive work has been carried out at low Reynolds numbers including Balint *et al* (1990) who studied statistical properties of velocity and vorticity fields at low Reynolds numbers. Ong and Wallace (1998) explored the joint probability of velocity and vorticity components at relatively low Reynolds numbers. Andreopoulos and Honkan (1997) measured near-wall vorticity, strain-rate and dissipation and in 2001 they examined vorticity stretching, and the velocity-gradient tensor (Andreopoulos and Honkan 2001).

Velocity and Vorticity studies at high Reynolds numbers are less abundant. Metzger and Klewicki (2000) examined velocity statistics at both low and very high Reynolds numbers. Maher (2002) investigated velocity, vorticity, and isotropy at very

high Reynolds numbers. Priyadarshana (2004) has examined very high Reynolds numbers at the SLTEST site and his thesis has documented velocity and vorticity products among other measurements.

3. Measurement Location for the Present Study

Experimental measurements were made at The Surface Layer and Environmental Science Test (SLTEST) site located on the U.S. Army Dugway Proving Ground in Utah's Great Salt Lake Desert. The Great Salt Lake and surrounding "salt flats" sit in the drying basin of what is believed to have once been a much larger body of water covering the entire region. The ancient basin features a flat surface with a very high salt content. The test site is located at $113^{\circ} 26.5' \text{ W } 40^{\circ} 8.1' \text{ N}$, in a region of the salt flat that is particularly smooth and flat with very little vegetation present. It lays approximately midway between bordering mountain ranges to the east and west. Prevailing wind conditions are northerly or southerly, with northerly winds more common. Long periods of relatively steady sustained wind speed and direction are characteristic of the location (Metzger and Klewicki 2000). The fetch leading to the site is extremely long and flat, extending to the North of the measurement location for more than 110km (SLTEST web site). Figure 3-1 is an illustration of showing the topology of the lakebed and the surrounding mountains.

Each morning and evening the ASL experiences a neutrally stable period as the temperature gradient transitions between positive and negative states. Under near neutral conditions, the ASL at the test site closely resembles a large canonical zero pressure gradient turbulent boundary layer. The duration of near-neutral thermal conditions ($|\zeta| < 0.1$) depends on the prevailing wind strength, cloud cover, and other

meteorological circumstances (Klewicki *et al* 1992). The University of Utah monitored thermal stability at the SLTEST site, using an array of digitally recorded resistance thermometers and sonic anemometers.

Observed surface roughness features were approximately 3mm in size, uniform in coverage, and randomly distributed. These observations agree well with other observations citing variations between 1mm and 3mm (SLTEST website). The downward shift in the mean velocity profile also indicates an equivalent sand-grain surface roughness of approximately 3mm. The roughness length at the site has been estimated to be 3×10^{-4} m (Metzger and Klewicki 2000). Surface dryness and cracking in the playa results in k_z values between 5 and 500 depending on the time of summer (provided by University of Utah).

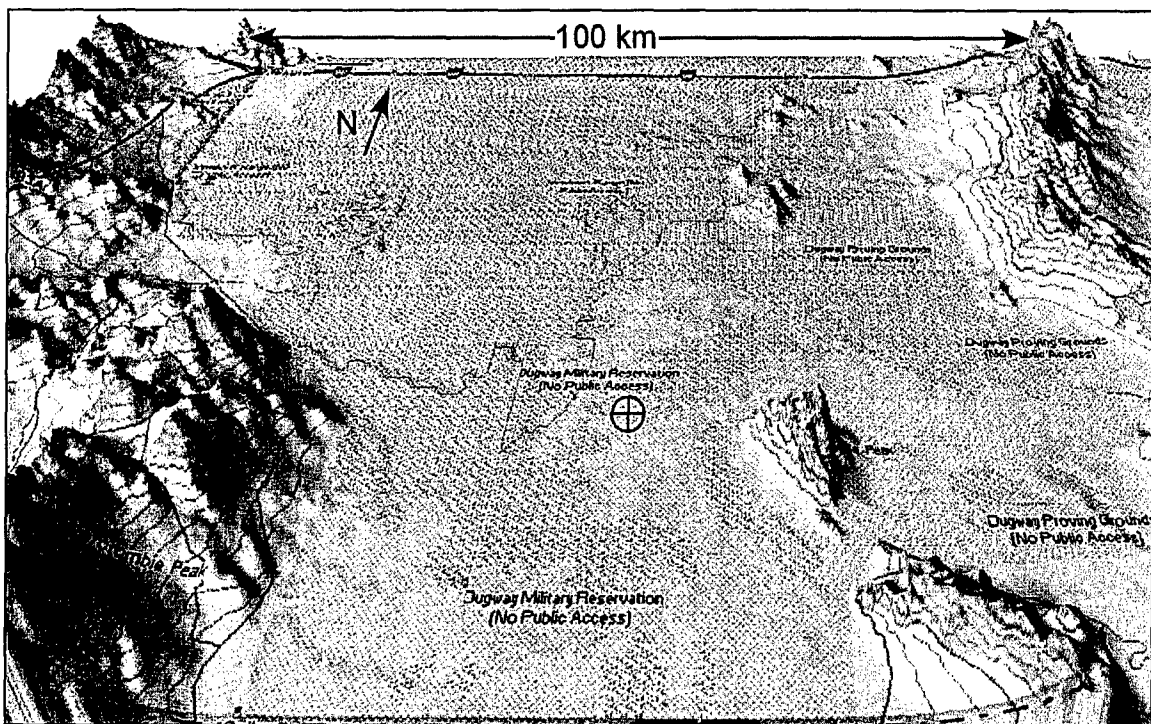


Figure 3-1 Topology of the SLTEST site

4. Experimental Methods

Heated-wire constant temperature (hot-wire) anemometry techniques were used to obtain high resolution measurements of velocity and vorticity from the atmospheric boundary layer during the evening period of neutral thermal stability.

4.1 Equipment

4.1.1 Data Cart and Measurement Equipment

A wheeled cart was used to deploy measurement equipment at the desert site. The cart also carried a small wind tunnel used for compact vorticity probe calibration. Onboard electronics included a conditioned power supply, BSI FieldGo PC, stepper motor controller (used to drive the wind tracking probe mount), a thermister unit, data acquisition board (for prevailing wind direction measurement), and the 100-kilohertz Pulse Width Modulated (PWM) constant temperature anemometer (CTA) system (Foss *et al* 1996). Details of the cart construction and onboard equipment can be found in the M.S. thesis of Mathew Maher (2002). Modifications were made to the cart in order to accommodate the PWM-CTA, to facilitate probe calibration, and to improve cooling. These modifications were designed and carried out by Alan Lawrenz of the Turbulent Shear Flows Laboratory at MSU. Figure 4-1 shows the cart and equipment in use at the test site.

The onboard wind tunnel was approximately 5 ft x 2 ft x 1 ft in size. The exhaust of two Dayton 4C015 Dual Shaded Pole Blowers situated on the pressure side was directed through a series of honeycomb and screen filter media, approximately 2 ft in

depth, as it passed into the plenum chamber. The plenum chamber was exhausted through a "duck lip" nozzle configuration with a contraction ratio of approximately 24 to 1. The nozzle outlet measured 1 in x 12 in. By throttling the blower, the onboard wind tunnel was able to achieve nozzle velocities over the range of 1-12 meters per second.

Two measurement fixtures were deployed to hold and position the sensors. One fixture was simply a fixed position tripod with a horizontal bar positioned at a height of 1.5 meters, to which an R.M. Young 03101-X 3-cup anemometer and 03101 electronic wind vane were mounted. The other fixture was specifically developed to hold and position the MSU Compact Vorticity Probes (CVP). This fixture featured a one meter rod protruding from a cube shaped base that enclosed a stepper motor and potentiometer for position measurement, and which enabled the rod to be rotated about its primary axis and controlled remotely via computer and stepper motor controller. The rotation of the rod was used in conjunction with wind vane measurements to align the compact vorticity probes with the mean wind flow and to record the low frequency shift in mean wind direction. This technique will be discussed in detail in a later section.



Figure 4-1 Photo of Data Cart and Measurement Equipment

4.1.2 MSU Compact Vorticity Probe

The probes used for this investigation were developed at Michigan State University by Foss and colleagues and are commonly referred to as the MSU Compact Vorticity Probe (MSU-CVP) (Wallace and Foss 1995). The probe is designed to measure two components of velocity and features an array of sensing elements that permits the calculation of one component of vorticity through the construction of a microcirculation domain.

The compact vorticity probes utilized in the present study are formed from an array of four hot-wires held at the tip of each probe as shown in figure 4-2. In this configuration, two hot-wires are parallel to one another and perpendicular to the probe body, while the other two wires cross to form an X as viewed from along the axis of either of the two parallel hot-wires. The parallel hot-wires of each probe will be referred to as "straight-wires." The wires that cross to form an X as viewed from along the axis of the straight-wires will be referred to as "X-wires." If the separation distance between the X-wires is negligible the wires may be thought of as being coplanar. For a 2D flow within this plane, the X-wires are capable of determining both speed and angle, from which two components of velocity may be derived.

The active segment of each hot-wire was made of 5 μm diameter tungsten filament approximately 1mm in length. On either side of the active segment, the tungsten filament was plated with copper which allowed the wire to be soldered onto jewelers broaches positioned at the tip of each probe. The separation distance between X-wires was nominally 1 mm. The separation distance between the straight-wires was also nominally 1 mm. However, the actual separation distance for straight-wires was precisely determined for each probe by incrementally traversing the probe across the shear layer from a slit jet. Each straight wire was used to measure the mean velocity profile as the probe traversed the shear layer. The distance that one velocity profile curve had to be shifted to superpose the other determined the separation distance between the straight-wires. In this way, separation distance was determined to within approximately 0.02 mm. Figure 4-3 is an illustration of the velocity profile measurements used to determine the separation distance.

The particular orientation of the 4-wire array allows each probe to measure two components of velocity as well as the vorticity vector normal to the plane of velocity measurement. For example, a probe situated to measure the u and v velocity components is also used to compute the ω_z vorticity component and will henceforth be referred to as an ω_z -probe.

The algorithm used to determine speed and angle will be elaborated upon in section 4.2.3. There are both speed and angle limitations to the probe. Accurate measurements can be made within a range of approximately $-36 \leq \gamma \leq 36$ where γ is the angle of the oncoming flow with respect to the axis of the probe body. The flow must be sufficiently fast to obey (0.18) (approximately 0.5 m/s), and must not be reversed in direction. Velocity results were obtained using flow speed measurements from the straight wires in conjunction with direction information from the X-array.

Turbulent flows are not two dimensional flows. The out-of-plane component of flow will result in error to measurements made using the CVP if it is not accounted for. Unfortunately, the problem of how to properly account for out-of-plane velocity components is complex. If ignored, out-of-plane velocity components will tend to cause an under-prediction of angle and an over-prediction of speed by the X-wire pair. The methodology used in the present study does not account for out-of-plane velocity components or resulting errors. However, careful probe orientation and file selection criteria minimize these effects. The spatial separation of the X-wires is another potential source of error that is not accounted for.

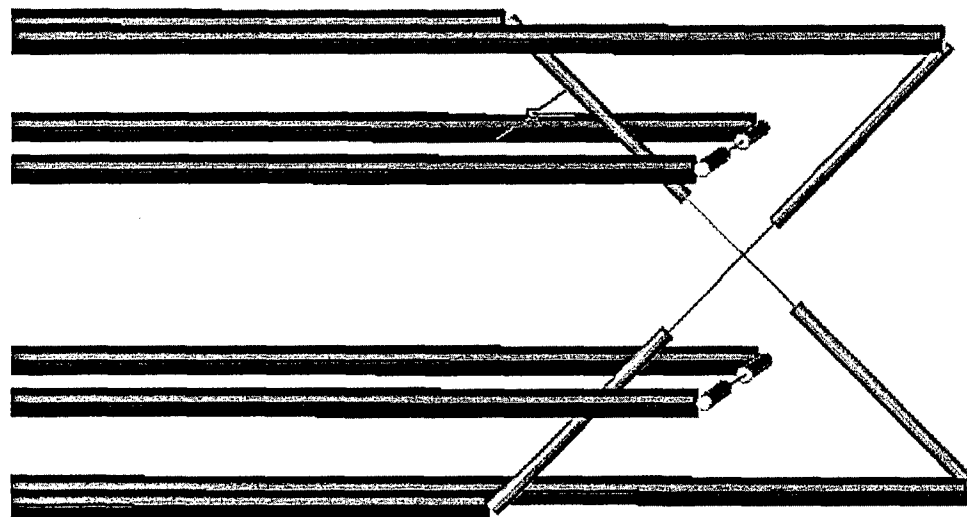


Figure 4-2 Illustration of hot-wire array used on the vorticity probes.

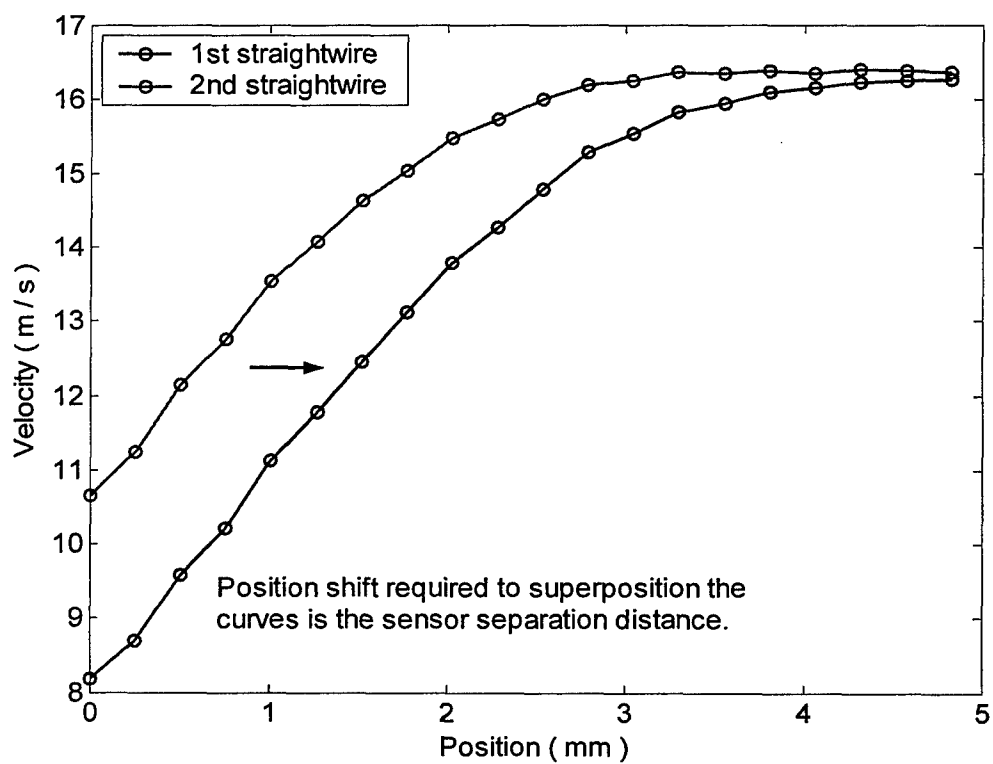


Figure 4-3 Straight-wire separation distance determination

4.1.3 The Pulse-Width Modulated Constant Temperature Anemometer

The Compact Vorticity Probes (CVPs) were operated by a 100-kilohertz Pulse Width Modulated Constant Temperature Anemometer (PWM-CTA) developed by Digital Flow Technologies, Inc. The PWM-CTA unit used for the present study was capable of sample rates up to 100 kHz and is equipped with 18 channels selectable for either hot-wire or A/D acquisition. As each CVP required the use of four channels, the unit was capable of driving up to four CVPs at once, leaving two channels available to sample other signals. The digitized data files were saved on a PC for storage. The PC also served as an interface device for operation of the PWM-CTA.

The PWM-CTA maintains a quasi-constant temperature by rapidly iterating through a cooling-followed-by-heating cycle. The heating pulse-width is modulated to maintain the quasi-constant wire temperature. The heating pulse-width (τ) is proportional to the input power of (0.18). The $\tau(t)$ time series obtained at sampling frequency f is not completely regular in time. A regularization scheme is employed to obtain corrected values for τ at frequency f . In practice, the need to regularize can largely be eliminated by sampling at a very high frequency. Comparisons between the original and regularized signals from the present research indicate that the differences between the two signals are negligible.

All experimental measurements were regularized according to methods developed by Foss and Hicks (2001). The regularization scheme is essentially an interpolation between a pair of τ values (τ_i and τ_{i+1}), acquired sequentially with an irregular time interval between data points, in order to find the appropriate value τ_t at the regular time

interval. Details of the operation and considerations for the development of the PWM-CTA are discussed in Foss *et al.* (1996).

4.2 Thermal Anemometry Techniques

The power required to maintain a thin segment of heated wire at some temperature greater than that of the surrounding fluid is related to the effective velocity magnitude Q and temperature T of the fluid by a form of *King's law of convective cooling* (Bernard and Wallace 2002):

$$Power \propto (T_{wire} - T(t)_{fluid}) \left(A(\gamma) + B(\gamma) Q(t)^{n(\gamma)} \right) \quad (0.12)$$

where A , B , and n are constants that must be determined for each hot-wire at angle γ (flow angle with respect to probe body in the present study). This relationship is the foundation for the commonly used heated-wire constant temperature anemometer (hot-wire) technique.

4.2.1 Hot-wire Calibration

A small wind tunnel mounted in the bottom section of the data cart served as a portable calibration unit for the hot-wires. The walls of the bottom section of the data cart, which partially enclosed the calibration unit, were made from a filter media with the intention of minimizing external flow disturbances that could adversely affect calibrations. The filter media also served to provide protection from particulate contamination that could potentially damage the hot-wires.

Air entered the calibration wind tunnel through the Dayton centrifugal blowers. A mechanized throttle between the blowers and the tunnel inlet allowed the flow rate to be varied in a slow quasi-steady manner. Flow then passed into a plenum chamber via a

series of filters, honeycomb straighteners, and screens. Air exited the plenum chamber to the atmosphere through a “duck-lip” nozzle configuration in the bottom section of the data cart. An MKS Baratron model 220BD differential pressure transducer was used to measure plenum pressure via a pressure tap. The transducer features a ± 1 Torr full scale range. The manufacturer stated resolution and accuracy are 0.01% of full scale and $\pm 0.15\%$ of the reading.

The calibration unit exit velocity adheres closely to the expected Bernoulli velocity. An experimentally determined correction factor was determined to account for a small ($< 2\%$) difference between the measured plenum pressure and the actual total pressure (as determined with a pitot tube). The corrected equation relating exit velocity to plenum pressure is given in (0.19).

$$Q_{exit} = \sqrt{2 \frac{1.011(P_{plenum} - P_{atmosphere})}{\rho}} \quad (0.13)$$

With this configuration, obtainable exit velocities ranged between approximately 1 m/s and 12 m/s. The CVPs were initially calibrated against the exit flow from the onboard wind tunnel over the full range of obtainable velocities, using (0.12) and (0.13).

As discussed in section 4.1.1, X-wires are used to measure speed and angle within a plane (the X-wires are coplanar if the separation distance is reduced to zero). Both straight-wires and X-wires were calibrated at 13 angles ranging from $-36 \leq \gamma \leq 36$ in 6 degree increments. Although straight-wires are often treated as insensitive to the normal flow direction, some degree of sensitivity was observed in the calibrations. Because of the need to maximize accuracy for reliable vorticity calculations, the straight-wires were also calibrated at each flow angle. As will be discussed, the processing

algorithms utilize these additional straight-wire calibrations to determine the flow speed as accurately as possible.

All hotwire calibration data were best fit in a least squares sense using an iterative routine to determine the coefficient n from (0.12). A thermister was used to measure changes in ambient temperature over time.

Figures 4-4 and 4-5 show the back-predicted velocity and flow angle as “measured” by the probes during calibration. That is, as a check of the calibration the calibration data were treated as measured data and processed as such. The fluctuations in flow angle seen in figures 4-4 and 4-5 could either be a result of noisy behavior of the sensors and related hardware or an indication of a noisy (not steady) calibration flow. It is believed that the latter is the case for the following reason.

The calibration data shown in figure 4-4 were taken during a period of relatively intense external flow. The plot reveals increased scatter in the calibration data as calibration speed decreases. In contrast, the calibration data of figure 4-5 were taken during a period of calm external winds, and does not reveal increased scatter in calibration flow angle even at low calibration unit flow velocities. It appears that high external wind speed can result in increased scatter at low speeds, caused by the interaction between the external flow and the calibration jet. At higher speeds, the calibration jet is less influenced by the external flow. This has a mitigating effect because higher calibration speeds were used during times of high external wind speed. Despite a higher calibration speed range, figures 4-4 and 4-5 indicate there was an appreciable increase in directional fluctuation of the calibration jet associated with high external wind speeds.

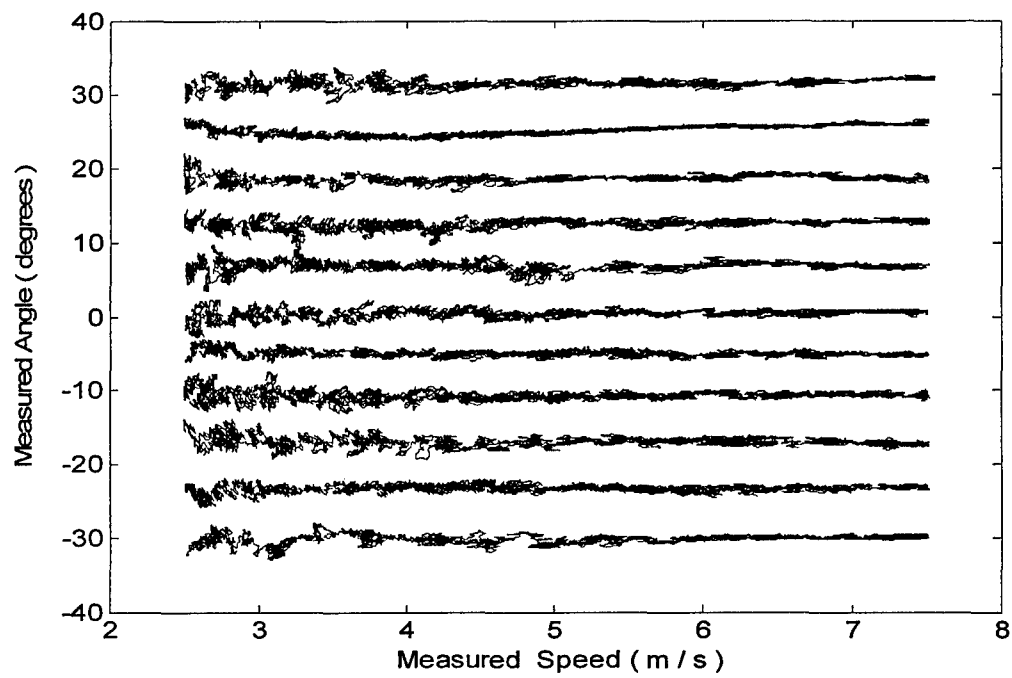


Figure 4-4 Typical post-calculated calibration data with high external wind speed

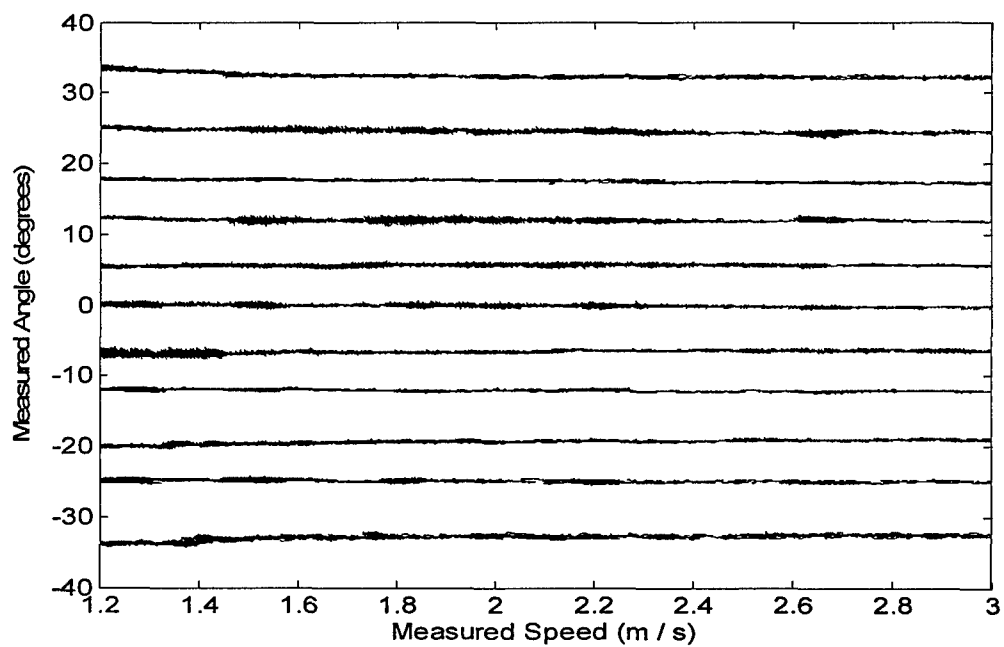


Figure 4-5 Typical post-calculated calibration data with low external wind speed

4.2.2 Hot-wire Calibration Correction

Histograms of the initial velocity calculations were used to determine the range of data over which to fit calibration coefficients. The measured boundary layer data were first processed utilizing the coefficients determined from the full speed-range calibration data. Histograms of measured flow speed were made from the initial results. Based on the histograms of measured flow speed, the calibration data range was truncated to exclude velocities not present in the measured flow data. The calibration coefficients were then recalculated to best fit the truncated calibration data. Finally, the measured data were reprocessed into velocity and vorticity time series using the improved calibration coefficients.

4.2.3 Velocity Processing Algorithm

Flow velocity was determined by rearranging equation (0.12) to express velocity as a function of both τ and angle γ . The two wires in the X-array are coupled by the fact that they must both agree on the velocity and angle of the flow being measured. This coupling is the basis for the modified 'speed wire/angle wire' (SWAW) method used in the present study to determine the correct speed and angle. This technique was originally developed by Morris (2002) as a variation on the method proposed by Foss. Per this method, at each point in the time series the predicted speed is determined as a function of angle for each of the wires in the X-array, $(Q_1, Q_2) = f(\gamma)$. The intersection of these two curves, where $Q_1(\gamma) = Q_2(\gamma)$, is the only location that satisfies the required agreement of speed and angle and thus represents the best estimate for the correct speed and angle. Figure 4-7 shows an example of how the curves for speed as a function of angle cross to determine the correct speed and angle reading at an instant in time.

Although the straight-wires are relatively insensitive to flow angle γ , this slight sensitivity should not be neglected. Incorporating this small sensitivity in the processing algorithm is necessary for an accurate evaluation of the velocity/vorticity products that serve as a primary objective for this research.

The flow angle $\gamma(t)$, as determined by the X-wires, was used to determine the nearest two calibration angles at time (t). Using coefficients at these angles, two velocities were calculated each representing the correct velocity at one of the two nearest calibration flow angles. A linear interpolation between these two velocities was performed to determine the correct measured velocity for the measured flow angle $\gamma(t)$.

Although this routine was somewhat cumbersome to implement, it better utilizes the available sensor data to achieve accuracy.

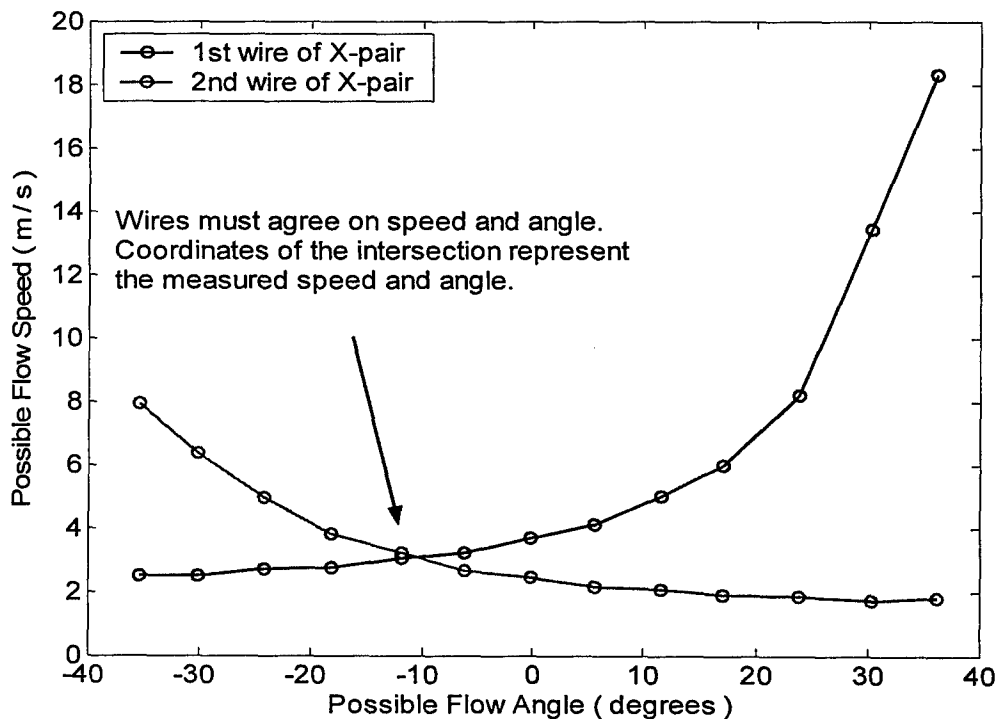


Figure 4-6 Hot-wires forming the X must agree on speed and angle

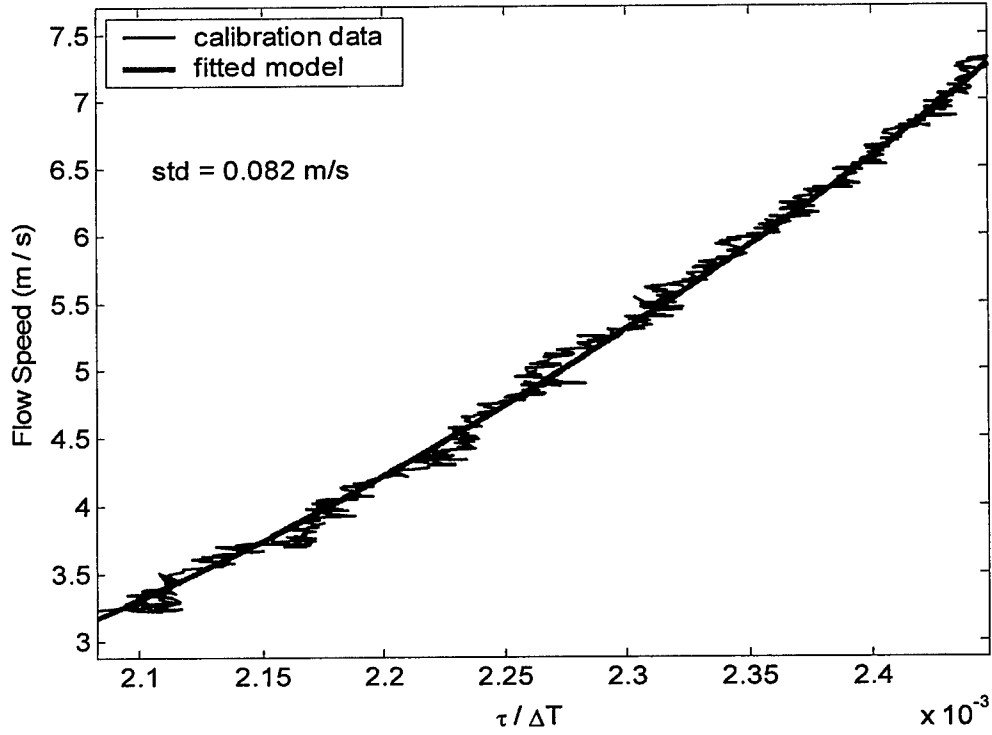


Figure 4-7 Example of Typical hot-wire calibration, x-wire at $\gamma = 12^\circ$

4.2.4 Vorticity Processing Algorithm

A microcirculation domain can be defined by constructing a parallelogram about the sensing region of the compact vorticity probe as illustrated in figure 4-10.

Streamlines of length Δs passing through the sensing region at angle ϕ are determined by

$$\Delta s(t_n) = \frac{1}{2f} \sum_{t_{n-1}}^{t_{n+1}} q_1(t) + q_2(t) \quad , \quad \phi(t_n) = \frac{1}{2i} \sum_{t_{n-1}}^{t_{n+1}} \gamma(t) \quad (0.14)$$

where q_1 and q_2 are the flow speeds at time (t) indicated by each of the straight wires and f is the sampling frequency.

The time step (i) in equation (0.14) is increased until a value is found such that the streamline length is greater than or equal to the straight-wire separation distance ($\Delta s \geq \Delta h$ at $i = M$). The average vorticity in the microcirculation region is then evaluated using 4.4, combined with the results of (0.14) evaluated at ($i = M$), to form:

$$\omega(t_n) = \frac{1}{2f\Delta s\Delta h} \sum_{t_{n-M}}^{t_{n+M}-1} (q_2^2(t) - q_1^2(t)) - \left(\frac{\sin \phi}{2\Delta s} \right) [q_1(t_{n+M}) + q_2(t_{n-M}) - q_1(t_{n+M}) - q_2(t_{n-M})] \quad (0.15)$$

Because q_1 and q_2 are speeds taken from the straight-wires on the vorticity probe, average differences between the two speeds contribute to an average vorticity by an amount inversely proportional to the separation distance of the sensors. Given the small spatial separation distance of the sensors and the accuracy of flow speed measurement, it was not possible to reliably measure mean vorticity. However, the sensitivity of hot-wires to speed fluctuations is sufficient to allow acceptably accurate measure of the vorticity fluctuations since these are much larger than the time-mean values (Wallace and Foss 1995).

Vorticity calculations are particularly sensitive to slight imperfections in hot-wire calibration because of the need to measure the velocity gradient between two sensors. The vorticity time series is highly irregular and marked with intermittent fluctuations many times the standard deviation in magnitude. While large fluctuations in vorticity may be measured accurately, the typical fluctuation is many times smaller in magnitude. Care must be taken when considering vorticity and particularly velocity-vorticity correlations, since it is possible for calibration imperfections to manifest themselves in a number of ways.

Cross-stream velocity (wall normal) and vorticity correlations may be used as an example of how small calibration imperfections may become manifest in the results. Cross-stream velocity components are found by multiplying the measured speed with $\sin(\phi)$ and are thus quite sensitive to the angle. Any slight sensitivity in the straight-wires to angle ϕ is amplified in inverse proportion to the sensor separation distance in the vorticity calculation. Since the separation distance must be small to resolve small scales of motion, and to prevent error in the estimation of vorticity, it is difficult to completely eliminate artificial correlation between cross-stream velocity and vorticity. The difficulty resolving small correlations between cross-stream velocity and vorticity makes it difficult to reliably determine the mean of the velocity-vorticity product. Straight-wire sensitivity to angle ϕ potentially introduces error to both the vorticity calculation and the velocity-vorticity correlation.

To minimize these effects, the straight-wires were calibrated over a range of angles. Similar to the X-wire processing routine, speed for each straight-wire was determined as a function of angle. The angle γ as determined from the X-wires was used to select the correct speed measured by each straight-wire by linearly interpolating between the two nearest calibration angles.

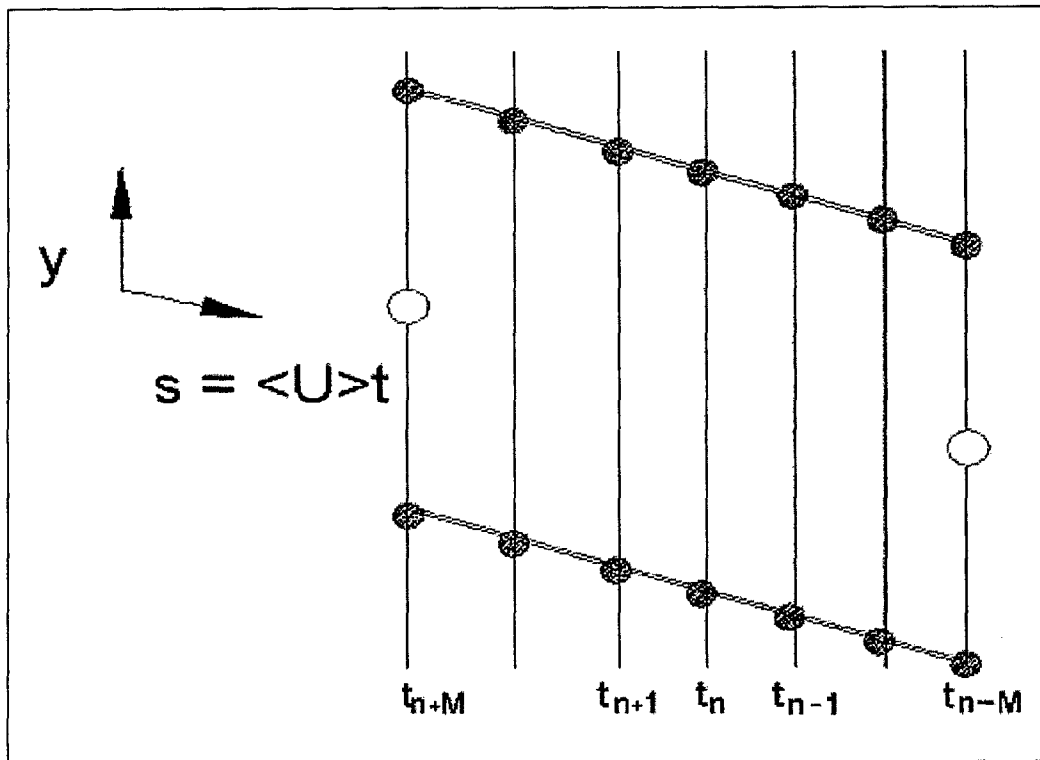


Figure 4-8 Schematic of microcirculation domain

4.3 Surface Shear-Stress Estimate

The $k_s^+ \approx 50$ data shown in figure 4.1 was collected at the SLTEST site by a team from the University of Utah in summer 2003. The collection occurred during the same week long period over which data were collected for the present study. It is unlikely that the surface roughness changed significantly over the one week period of the present study, making comparison possible on the basis of a constant surface roughness.

For a known surface roughness, (0.8) and (0.9) provide a means of estimating the surface shear-stress (τ_s) from \bar{U} and y and k_s . In the present study τ_s was not measured directly; hence, \bar{U} and y and k_s were used to estimate the values for τ_s on 4 and 13 June 2003.

directly; hence, \overline{U} and y and k_s were used to estimate the values for τ_s on 4 and 13 June 2003.

Sonic-anemometers operated by the University of Utah team provided a good estimate of τ_s during their measurements. By comparing the transitionally rough-wall profile ($k_s^+ \approx 50$) from the 2003 SLTEST site data and the smooth-wall profile, it is seen from (0.9) that the equivalent sand-grain roughness can be estimated, a number that works out to be approximately $k_s \approx 2.9mm$. This estimate is used in the present study to represent the surface roughness at the SLTEST site. The estimate agrees well with observed surface conditions.

The Reynolds stress ($-\overline{uv}$) is also related to the surface shear-stress. The Reynolds stress is nearly constant for a range about its peak value, which is approximately located at $y_p^+ = 2\sqrt{\delta^+}$ (Sreenivasan and Hak 1989). The total stress is nearly constant over a distance (extending out from the wall) that increases with Re and includes y_p (Bernard and Wallace 2002). The Reynolds stress dominates the total stress through much of the constant stress region (viscous stresses dominate very close to the wall). It follows that in the vicinity of y_p , the Reynolds stress serves as a good estimate of the total stress, which in turn is very nearly equivalent to the surface shear-stress.

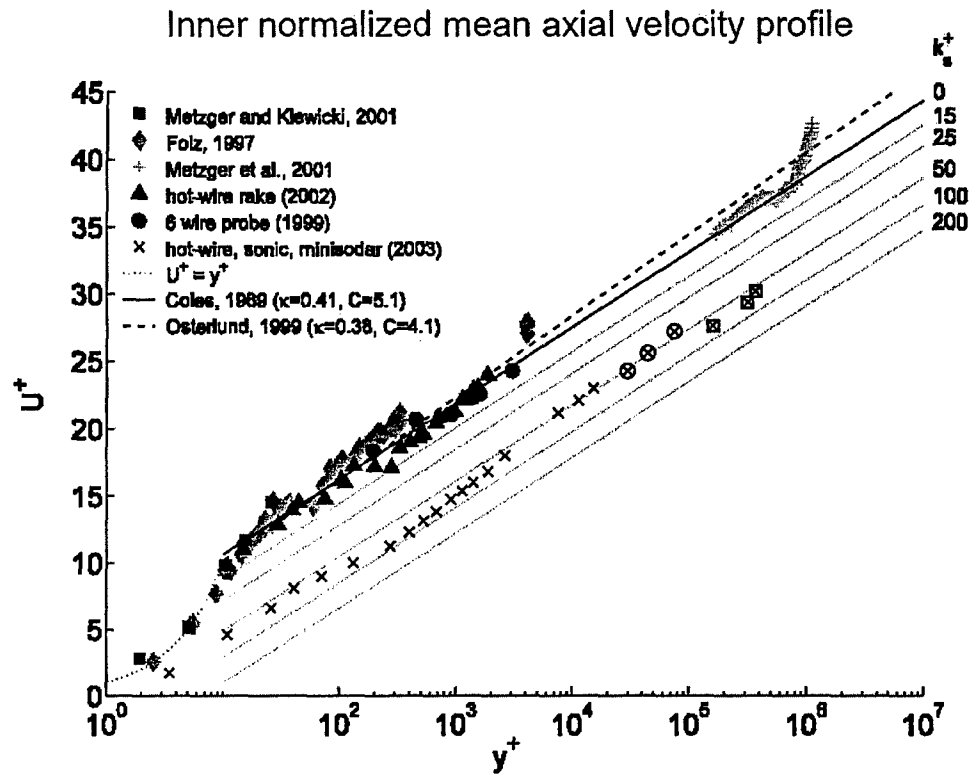


Figure 4-9 Velocity profile at SLTEST site [Metzger, University of Utah, 2004]
(Data for $k_s^+ = 50$ from SLTEST site in summer, 2003)

4.4 Experimental Procedure

Each day the targeted data acquisition window occurred within the evening period of neutral thermal stability. The objective was to deploy an array consisting of four compact vorticity probes, three of which were aligned to measure the ω_z vorticity component at heights of 13, 15, and 19 cm above the desert floor. The fourth compact vorticity probe was oriented so as to measure the ω_y component of vorticity and was positioned 15 cm above the desert floor. The probes oriented to measure ω_z also measured the streamwise (u) and wall normal (v) velocity components. The probe

oriented to measure ω_y , also measured the streamwise (u) and transverse (w) components of velocity. Because of unexpected circumstances, all four probes were not successfully deployed each day.

Prior to the first evening of data collection, the wind tracking probe mount and tripod mount for the wind vane and 3-cup anemometer were positioned at the site on the north side of the access road in anticipation of a prevailing northerly wind direction.

The box shaped base for the probe mount, which housed the electronic apparatus used to rotate the mount, was carefully buried such that its upper surface was flush with the desert playa and the playa smoothed so as to minimize the disturbance of the flow. The mounting rod protruded vertically above the plane of the desert floor. Figure 4-10 shows the probe mount positioned at the test site. In the event of southerly prevailing wind direction, a secondary probe mount was available but was not equipped for electronic wind tracking. However, no data were collected with southerly prevailing winds. The location of the probe mount and tripod was chosen to minimize the chance of obstruction or uncharacteristic upstream disturbances that would have resulted from other on-site activity.

Each day the CVPs were calibrated prior to data collection using the wind tunnel on the data cart. After calibration, the probes were removed from the calibration unit and attached to the pre-positioned probe mount for atmospheric measurements. The three cup anemometer and electronic wind vane were positioned atop the tripod at a sensing height of 1.8 meters; see Fig. 4-11. The electronic wind vane was referenced to magnetic north as were the CVPs aboard the wind-tracking mount. A thermister was used to monitor air

temperature in the calibration unit during calibration. It was then relocated to measure air temperature in the vicinity of the CVPs during atmospheric measurements.

CVP data were acquired at 50 kHz on all channels for 18 to 30 seconds per data file. Software issues and PWM sample and hold hardware determined the maximum continuous collection period. These data were written to disk prior to the next continuous acquisition period. The file writing time between continuous acquisition periods was only a few seconds in duration.

In addition to the hot-wire channels, the thermister channel and the 3-cup anemometer channel were also sampled. The thermister data were used to compensate the hot-wire calibrations for changes in ambient temperature. The 3-cup anemometer was used to monitor prevailing wind conditions.

Low frequency fluctuations in the prevailing wind direction over the duration of the measurement period were expected to exceed the acceptable range for measurement with a fixed position vorticity probe. It was therefore necessary to periodically adjust the orientation of the probes so that they were aligned with the local mean wind direction. For this reason, a second data acquisition system was used to monitor and track the prevailing wind direction and this system was run in parallel with the PWM-CTA.

This tracking system monitored the electronic wind vane placed at a height of 1.8 meters. The wind vane signal was sampled for 20 seconds at a rate of 200 Hz. This acquisition period was concurrent with the first 20 seconds of each PWM-CTA acquisition period. The sampled wind vane signal was used as feedback to control the mechanized probe mount in order to point the probes into the wind. The probe direction adjustments were made during the PWM file writing period which was already a

necessary interruption to the continuous data collection. The amount to adjust the direction of the probes between files was determined by comparing the probe direction with the average wind vane direction over the previous continuous acquisition period. Thus a phase lag of approximately 30 seconds existed between wind vane measurement and probe alignment. The direction that the probes were pointed during each data acquisition period, in relation to magnetic north, was recorded in a data file.

The effectiveness of the wind tracking was determined by examining the histogram of wind angle with respect to the ω_y vorticity probe, as determined from the collected data. For each data file, if the mean wind angle with respect to the probe body was found to exceed ± 5 degrees then the data from that file were not incorporated into the processed results. This was done to ensure that the fluctuating velocity components were not truncated at the extreme angles because of probe angle limitations. This also ensured that errors associated with out-of-plane measurements were minimized.

Unless otherwise noted, post-calibrations of the hot-wires were made upon the completion of the data collection window each day.



Figure 4-10 Photo of deployed probes and wind-tracking probe holding assembly.



Figure 4-11 Photo of mounted probes, tripod, and windvane.

5. Results and Discussion

Measured properties of the mean flow will be presented in several forms. In addition to dimensional measurements, inner-normalized results are presented.

Because the atmospheric boundary layer is not statistically stationary, convergence of statistical data does not occur. However, over the duration of the data acquisition periods the prevailing wind direction and speed remained relatively steady (figures 5-1, 5-2, 5-3, and 5-4).

The largest scales of motion are on the order of the size of the boundary layer itself. Therefore, a large number of boundary layer thicknesses must be sampled in order to ensure statistical significance. Since turbulent properties are increasingly isotropic at smaller length scales, the statistical contributions of small scale motions should converge much faster than the contributions of larger scales motions. Therefore, high wavenumber contributions converge at a faster rate than low wavenumber contributions. It can thus be presumed that statistical properties that demonstrate large contributions at high wavenumbers and only small contributions from low wavenumbers may be statistically converged even though other statistical properties of the flow (that depend on contributions from low wavenumbers) are not.

As previously noted, the direction of the probe body was at all times referenced to magnetic North. The flow angle γ as measured by the ω_y probe is the horizontal flow direction in relation to the probe body. Records of both angles permitted wind direction to be determined with respect to magnetic north.

Although the mean wind direction appeared to be holding relatively steady during each of the datasets (as compared to some of the periods not included in the reported results), closer examination revealed the presence of fluctuations acting on very long time-scales. This is to be expected because the atmospheric boundary layer is not a statistically stationary flow. Because the statistics of interest require the identification of a mean, it is necessary to evaluate the mean over some finite interval of time. It is clear that over too short a duration the results may not converge. However, it is also possible to choose a duration that is so long that the flow no longer properly resembles a canonical boundary layer.

Although prevailing wind conditions were relatively steady during the measurement intervals, mean wind speed and flow direction trends were removed by a linear fit against data acquisition file number (see figures 5.1 and 5.3). The scatter in the mean wind direction and velocity from file record to file record indicates the presence of low frequency fluctuations that do not converge within a single record.

As will be shown, using a linear fit to represent the mean velocity magnitude and the transverse flow angle leads to a large transverse fluctuation intensity (w') that is nearly the same as the streamwise fluctuation intensity (u'). Although the ASL resembles a canonical boundary layer, low frequency changes in mean wind direction may be present that are non-canonical. It is argued that this is most easily noticed in the transverse direction, while the wall-normal and streamwise quantities are less affected.

This assertion was investigated by processing the data two ways. First, the linear fits of average speed and direction were used to determine U . Second, U was found using the linear fit for speed, but with the direction of U taken to vary from file to file such that

\overline{w} is zero for each file. Using the second method, transverse fluctuation levels were more consistent with other studies and conventional understanding while other statistical quantities were generally unchanged. A comparison of results obtained using each processing method is presented in table 5-1. Because the differences were limited primarily to w' , and to ensure a consistent comparison between measurement days (winds on June 4th were not as consistent in direction as on June 13th), the method using local means for the U-direction was chosen as that most consistent with canonical flow.

Results presented in this report were processed taking the mean direction of each data file to represent the U direction, in this method the flow direction changes with the local mean direction.

5.1 Daily Specifics

Velocity and vorticity measurements were successfully acquired on the evenings of June 4th and 13th of 2003 at wall-normal heights of nominally $y^+ = 2150$ and $y^+ = 810$ respectively. The following sections describe conditions and circumstances that are unique to each of the days.

5.1.1 June 13th, 2003 ($y^+ = 810$)

The June 13th dataset includes results from two CVPs. These probes were positioned at a wall-normal height of 15 cm, with one oriented to measure ω_z and the other to measure ω_y .

Data were collected for 322 acquisition periods, each 30 seconds in duration. Of the 322 data files acquired on this evening, the subset of primary importance consists of files 287 through 322, over which wind speed and direction remained consistent and

nearly neutral thermal stability was observed. Using $\delta = 150m$ as an approximation for boundary layer thickness, data in the neutral subset were collected over a length of approximately 13 boundary layer thicknesses.

On this evening data collection began under unstable thermal conditions (negative thermal gradient in wall normal direction) and ended under conditions that were nearly neutral (a slight positive temperature gradient was present at the time of the final record). The thermal stability parameter was not available on this date. However, temperature readings from an array of vertically spaced quartz thermometers were periodically noted. The precise spacing of the thermometers has not been determined albeit the nominal spacing is 10cm. The readings are a reliable indicator of the trend in the temperature gradient and are a reliable indicator of qualitative stability (i.e. unstable or stable).

Meteorological data from nearby Army weather stations were also available. These data included temperature readings from an upper and lower elevation. Once again, the sensor separation distance was not available. The weather station data supports the trend and indicates the same timing for the transition through neutral conditions on the evening of June 13th, 2003.

On-site measurements indicate the transition through neutral conditions occurred between 8:20pm and 8:56pm MDT. Data from a nearby Army weather station show the transition to occur between 8:40pm and 9:00pm MDT. Results presented in this chapter at $y^+ = 810$ were collected during the neutral period on this date. Starting and ending times for the presented data are 8:34pm and 9:00pm MDT respectively.

Significant differences were observed between the pre and post hot-wire calibrations. Because a long time interval passed between pre and post calibrations on

this date, the drift in the calibrations is not surprising. Rather than attempting to combine calibrations, which is a technique that is sometimes used (incorporates pre and post calibration data into a single calibration), only the post calibration was used in computation of these results.

There are several reasons for using only the post-calibration. The neutral period of interest occurred towards the end of the data collection period which is much nearer the post-calibration period than the pre-calibration. The mean wind speeds during the neutral period were relatively slow compared to the wind speeds earlier in the day. As noted in section 4.2.1, high external wind speeds adversely affect the calibration unit flow. The external wind speed was much lower during the post-calibration than the pre-calibration which was favorable for calibration.

The mean wind direction was relatively steady during the neutral period of June 13th. The wind-tracking system was used, and adjustments between files were generally small. Figure 5.1 and 5.2 show direction and speed trends for the prevailing wind conditions. Although the mean wind speed during this period was relatively consistent and did not undergo any dramatic changes, a clear trend of decreasing speed over time was observed. The time series was detrended using a linear fit to the data presented in figure 5-2. Instantaneous fluctuations in velocity magnitude were obtained by subtracting the local mean from the instantaneous reading, where the local mean varies over time to reflect the observed trend. A similar method was used to detrend the mean wind direction (figure 5-1).

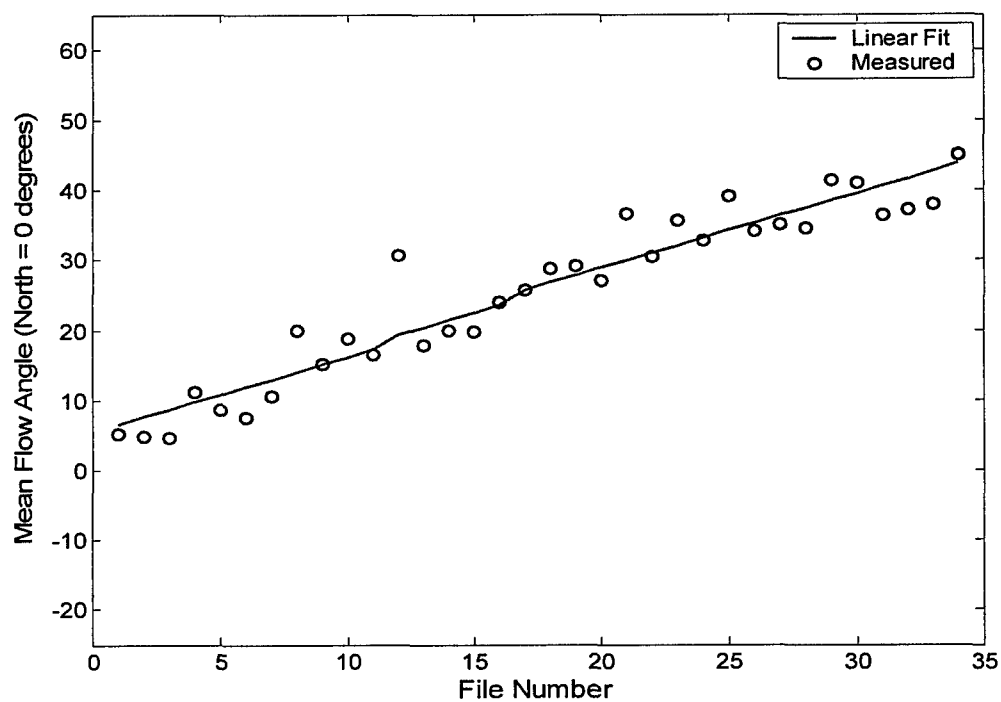


**Figure 5-1 Wind direction with respect to magnetic North. $y+ = 810$
June 13, 2003 8:45pm – 9:00pm MDT**

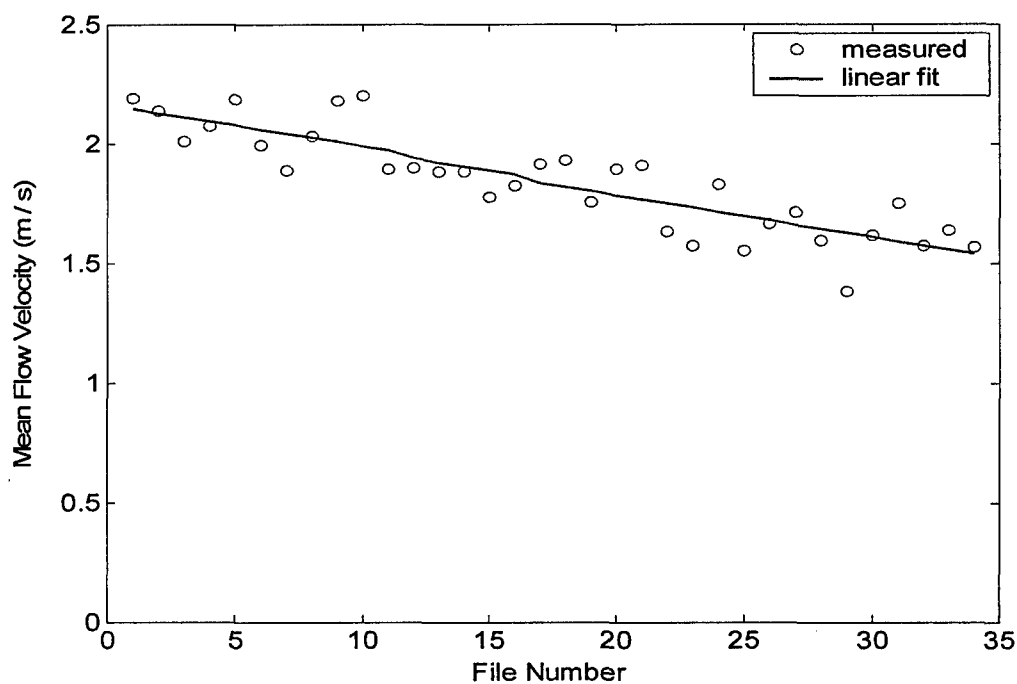


**Figure 5-2 Mean wind speed and trend line over collection period at $y+ = 810$
June 13, 2006 8:45pm – 9:00pm MDT**

5.1.2 June 4th, 2003 ($y^+ = 2150$, $y^+ = 1850$)

The June 4th dataset includes results from three compact vorticity probes: two ω_z - probes deployed at heights of 13 cm and 15 cm as well as one ω_y -probe deployed at a height of 15 cm. Data were collected for 47 acquisition periods each 18 seconds in duration. Using $\delta = 150m$ as an approximation for boundary layer thickness, data were collected under neutral conditions over a length of approximately 26 boundary layer thicknesses.

Data collection ceased prematurely because of hardware malfunction within the acquisition system. This malfunction also prohibited post-calibration of the probes on this day. A fourth ω_z -probe was deployed at $y=19$ cm on the evening of June 4th, but it only survived for six acquisition periods, each 18 seconds in duration. Hence, results from this probe were not significant and were of limited utility.

As seen in figures 5-3 and 5-4, the prevailing wind direction and speed was less steady on June 4th. When the average flow direction during each acquisition period is taken to be the x-direction the resulting flow statistics are somewhat different than if the mean flow direction is determined with respect to magnetic North. Significantly, a difference is apparent in the calculated magnitude of the w -component fluctuations. In North-referenced coordinates, the root mean squared fluctuation in w is almost as large as the u component fluctuations. There are a couple of problems with this. First, this result is not expected from our knowledge of how turbulence is generated. Second, these statistics do not agree well with other studies of near-wall boundary layer turbulence

intensities. Better agreement is achieved if the mean flow direction for each file is taken to represent the x -direction. Using this method, which is in agreement with the data processing for the 13 June records, the relative turbulence intensities of u , v , and w components are in much better agreement with other results. Hence, the results reported in this study are arrived at by taking the mean direction of each file to represent the actual mean flow direction. It is believed these results are more consistent with what would be seen in a canonical boundary layer.

Although the mean wind speed during this period was relatively consistent and did not undergo any dramatic changes, a clear trend of decreasing speed over time was observed. The velocity time series was detrended using a linear fit to the data presented in figure 5-2. Instantaneous fluctuations were obtained by subtracting the local mean from the instantaneous reading, where the local mean varies over time to reflect the observed trend. Again, a similar method was used to detrend the mean wind direction (figure 5-3).

Thermal stability was monitored via on-site quartz thermometers and cross-checked with sensor readings from a nearby Army weather station. The on-site thermometer array indicated the transition through neutral conditions occurred between 8:15pm and 8:30pm MDT. Army weather station data indicate the transition occurred between 8:20pm and 8:40pm MDT. Results presented in this chapter at $y^+ = 2150$ and $y^+ = 1860$ were collected on this date between 7:40pm and 8:11pm MDT. Nearly neutral thermal conditions were observed over the entire measurement period.

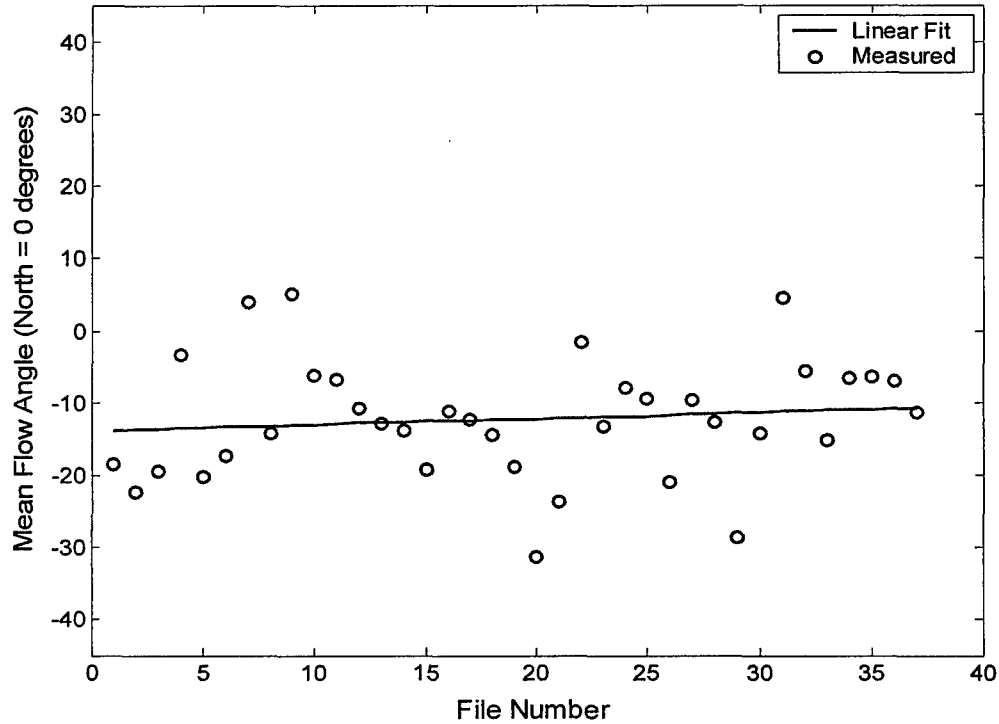


**Figure 5-3 Wind direction with respect to magnetic North. $y+ = 2150$
June 4, 2006 7:40pm – 8:11pm MDT**

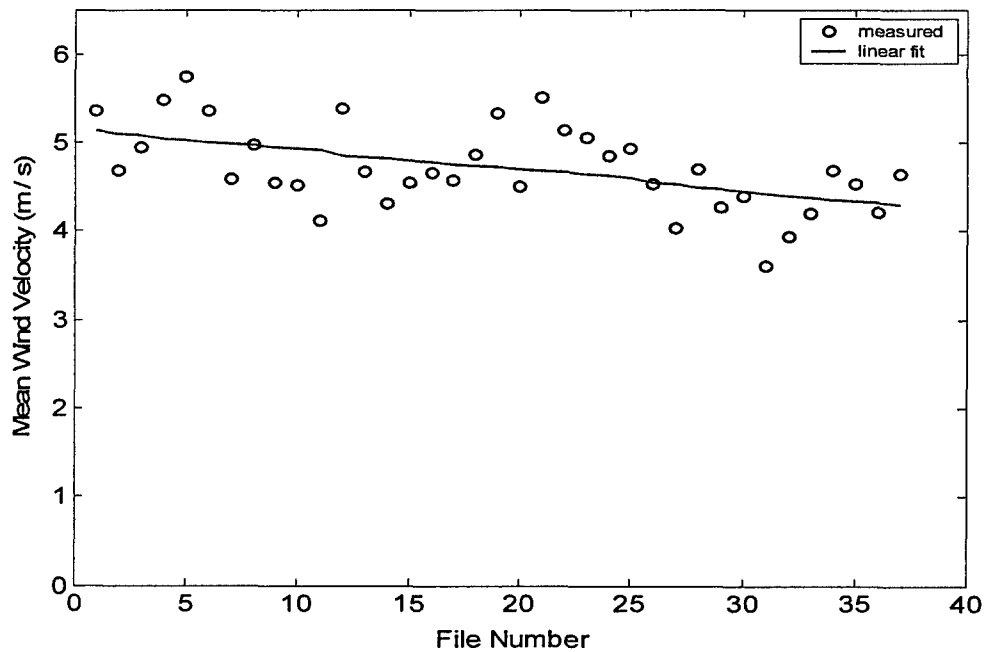


**Figure 5-4 Mean wind speed data and trend line over collection period at $y+ = 2150$
June 4, 2006 7:40pm – 8:11pm MDT**

5.2 Velocity Measurements

5.2.1 Comparison between using local and linear-fit for direction of U

Methods of determining mean flow angle and wind speed are discussed at the beginning of this chapter (Section 5.0).

A comparison between results using the locally determined mean direction (varying each data file) and a linear-fit for mean wind direction is shown in table 5-1. It is clear that transverse fluctuation intensity w' is significantly larger when file to file fluctuations are included, similar in intensity to u' . Importantly, it is revealed that $\overline{w\omega_y}$ is the same using either method while $(w\omega_y)'$ increases in nearly proportionately with w' . These results suggest that low-frequency fluctuations do not contribute to the velocity-vorticity correlation but can contribute to the intensity of the fluctuation of the product.

Statistical results presented in the following sections make use of a locally determined flow direction at each data file taken to represent the direction of U.

Table 5-1 Comparison between methods of determining direction of U.

Data Set and Method	u'	w'	$\overline{w\omega_y}$	$(w\omega_y)'$
June 13 th , $y^+ = 810$ U: Trendline	0.77 m/s	0.76 m/s	2.2	67.9
June 13 th , $y^+ = 810$ U: Local Mean	0.74 m/s	0.55 m/s	2.2	47.7
June 4 th , $y^+ = 2150$ U: Trendline	0.25 m/s	0.21 m/s	-2.3	7.48
June 4 th , $y^+ = 2150$ U: Local Mean	0.25 m/s	0.18 m/s	-2.1	6.5

5.2.2 Tabulated Statistics

Statistical results of velocity measurements are listed in dimensional form in table 5.2. Inner normalized results appear in table 5.3.

As noted in section 4.3, the surface shear-stress used for normalization in the present study was obtained using 2.12 and 2.13 for a known surface roughness. The roughness used was determined from data collected by the University of Utah. The measured Reynolds-stress and the estimated surface shear stress agree relatively well, with the Reynolds stress in each case being somewhat lower than the surface shear-stress. This would indicate a slight reduction in the total stress from that present at the wall, although this could also be the result of slightly over-estimating the surface roughness.

Fluctuation intensities generally fall into agreement with other high Re results including Maher (2002) and Priyadarshana *et al* 2006, albeit the scatter in the inner-normalized data is at a level which precludes "precise comparisons."

Table 5-2 Dimensional Velocity Statistics

	y+ = 810	y+ = 1860	y+ = 2150	units
y	0.15	0.13	0.15	m
v	1.85E-05	1.85E-05	1.85E-05	m ² /s
U_{τ}^*	0.100	0.265	0.265	m/s
$\sqrt{-\overline{uv}}$	0.089	0.243	0.232	m/s
\overline{U}	1.8	4.65	4.76	m/s
u'	0.25	0.75	0.74	m/s
v'	0.11	0.31	0.33	m/s
w'	0.18	n/a	0.55	m/s
\overline{uv}	-0.008	-0.059	-0.054	m ² /s ²
η_u	7.70E-04	3.33E-04	3.42E-04	m
η_v	8.40E-04	3.75E-04	3.79E-04	m
η_w	8.30E-04	n/a	3.73E-04	m
λ_u	0.044	0.025	0.026	m
λ_v	0.016	0.009	0.010	m
λ_w	0.025	n/a	0.016	m

* U_{τ} derived on June 13th from velocity profile and known surface roughness

Table 5-3 Inner Normalized Velocity Statistics

	y+ = 810	y+ = 1860	y+ = 2150
y+	811	1862	2149
U^+	18	17.55	17.96
u'^+	2.5	2.83	2.79
v'^+	1.1	1.17	1.25
w'^+	1.8	n/a	2.08
\overline{uv}^+	-0.80	-0.84	-0.77

Table 5-4 Kinematic Reynolds Shear Stress Values

	y+ = 810	y+ = 1860	y+ = 2150	units
$\overline{-uv}$	0.008	0.059	0.054	m/s
$\frac{\overline{-uv}}{\overline{u'v'}}$	0.29	0.25	0.22	
$\frac{\overline{-uv}}{\overline{U_{\tau}^2}}$	0.80	0.84	0.77	

5.2.3 Probability Density

The joint probability distributions of u and v as well as u and w are shown in figures 5-5 through 5-9 for $y^+ = 810$ and $y^+ = 2150$. The weighted probability densities are shown in figures 5-10 through 5-14.

As expected, a strong diagonality appears in plots of u and v which is indicative of and consistent with the kinematic Reynolds shear stress. Quadrants two and four are associated with a negative contribution to the mean. The diagonal bias is present across a broad range of iso-contour levels but appears to decrease somewhat as the probability level increases near the (0,0) origin. This observation suggests a correlation between "small" fluctuation levels and a decreased correlation between u and v . The decrease in diagonality at low fluctuation magnitudes is more prevalent at $y^+ = 2150$ than at $y^+ = 810$, perhaps owing to being a farther normalized distance from the wall.

The weighted joint probability distribution is an indication of the relative significance of fluctuations in contribution to the mean of the distribution. While fluctuations of small magnitude occur more often than fluctuations of greater magnitude, the contribution to the mean depends on both the magnitude of the fluctuation and the probability of that fluctuation. As shown in the plots of the weighted joint probability in u and v , each quadrant represents a grouping of turbulent fluctuations that contributes either positively or negatively to the kinematic Reynolds stress. Contributions to the Reynolds shear stress do not come primarily from the small fluctuations, rather from intermediate and large fluctuation levels. The dominant fluctuation size appears to be approximately one standard deviation in magnitude in all quadrants, with negative contributions being larger than positive contributions at intermediate and large fluctuation

magnitudes. An increased level of contribution at large fluctuation magnitudes is noted in quadrant two for $y^+ = 2150$ and $y^+ = 1860$ as compared to the $y^+ = 810$ case.

Joint probability distribution of u and w were not expected to exhibit a component of diagonality. The unexpected result seen at $y^+ = 810$ could have two causes. It is either a result of the incorrect selection of the mean wind direction (see Section 5.0) or calibration drift which caused a systematic correlation to exist between flow speed and flow angle about zero. At $y^+ = 2150$ the probability distributions behave as expected with only a slight contribution to a non-zero \overline{uw} product.

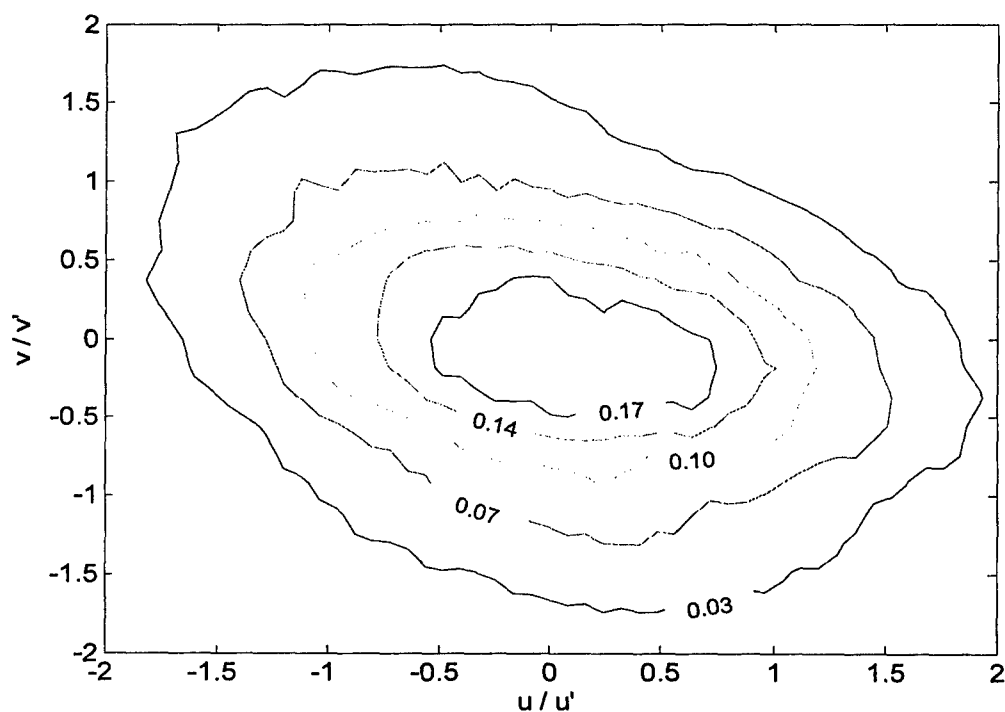


Figure 5-5 Joint probability density of u and v at $y^+ = 810$.

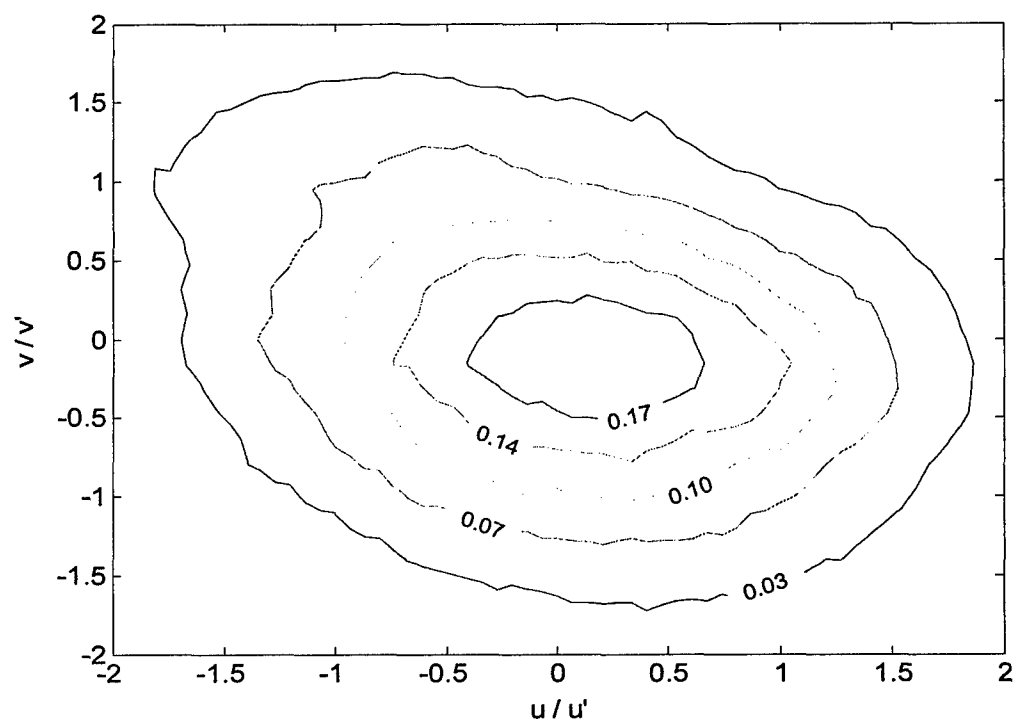


Figure 5-6 Joint probability density of u and v at $y^+ = 1860$

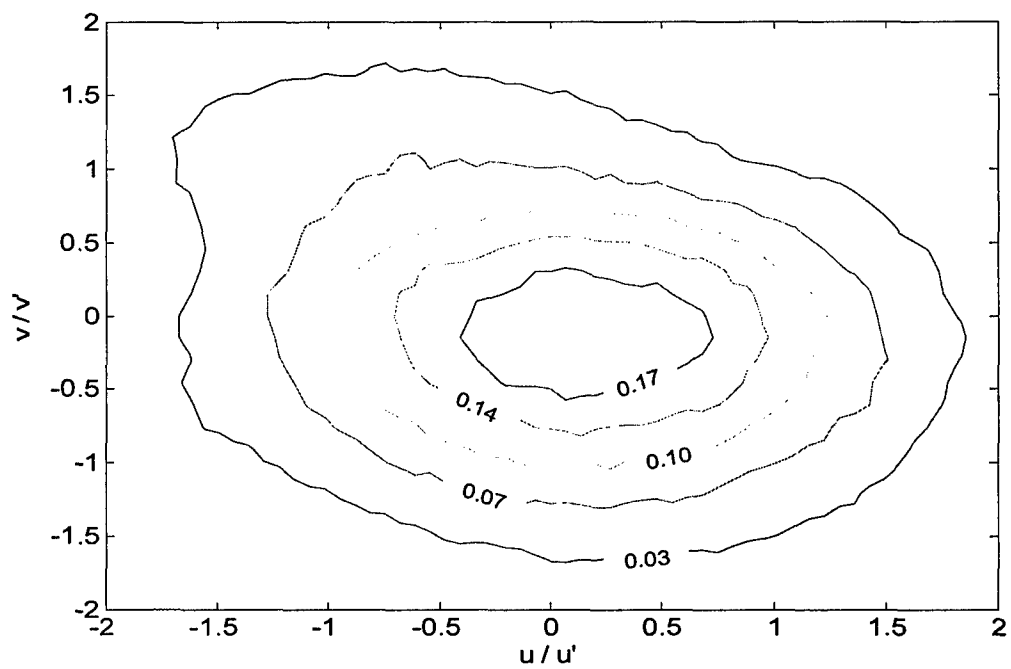


Figure 5-7 Joint probability density of u and v at $y^+ = 2150$

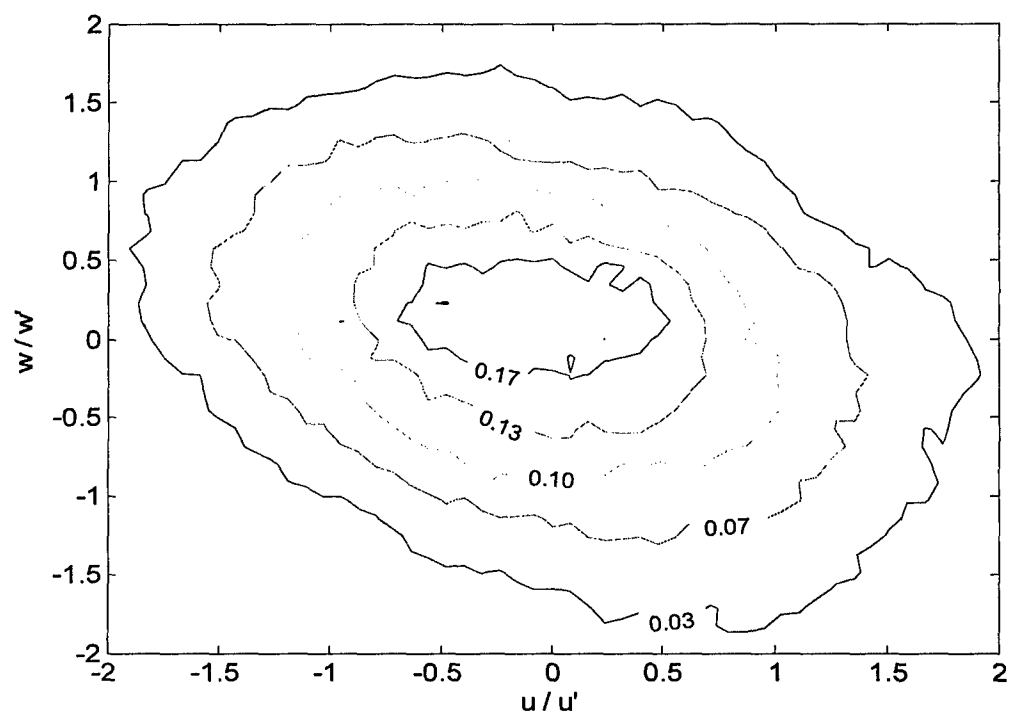


Figure 5-8 Joint probability density of u and w at $y^+ = 810$

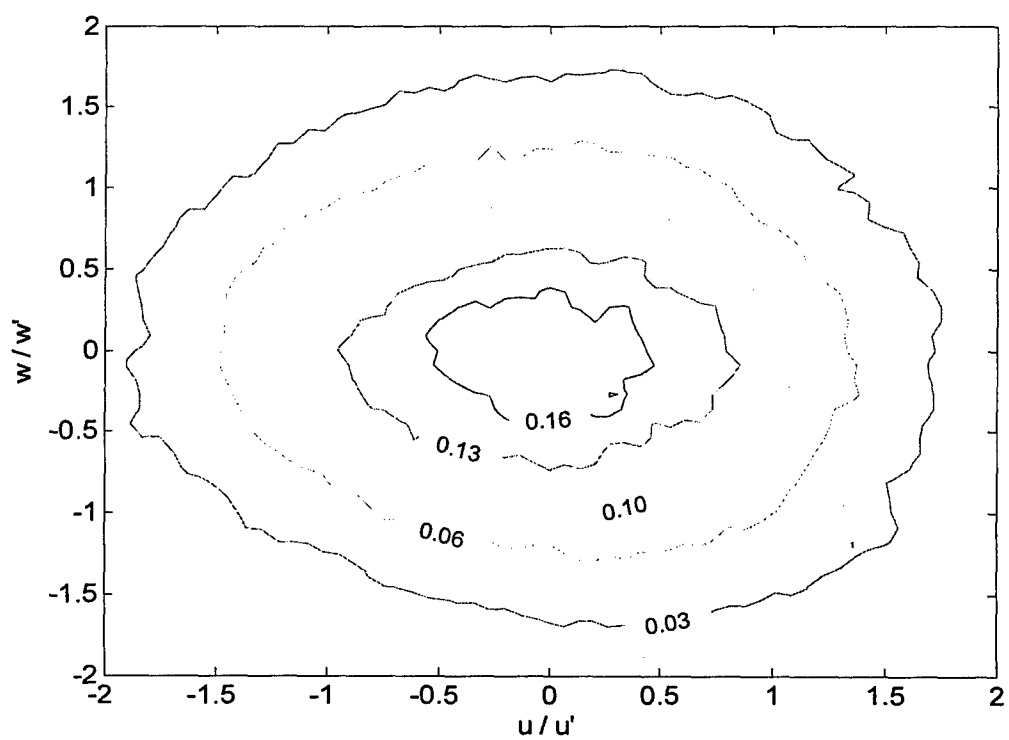


Figure 5-9 Joint probability density of u and w at $y^+ = 2150$

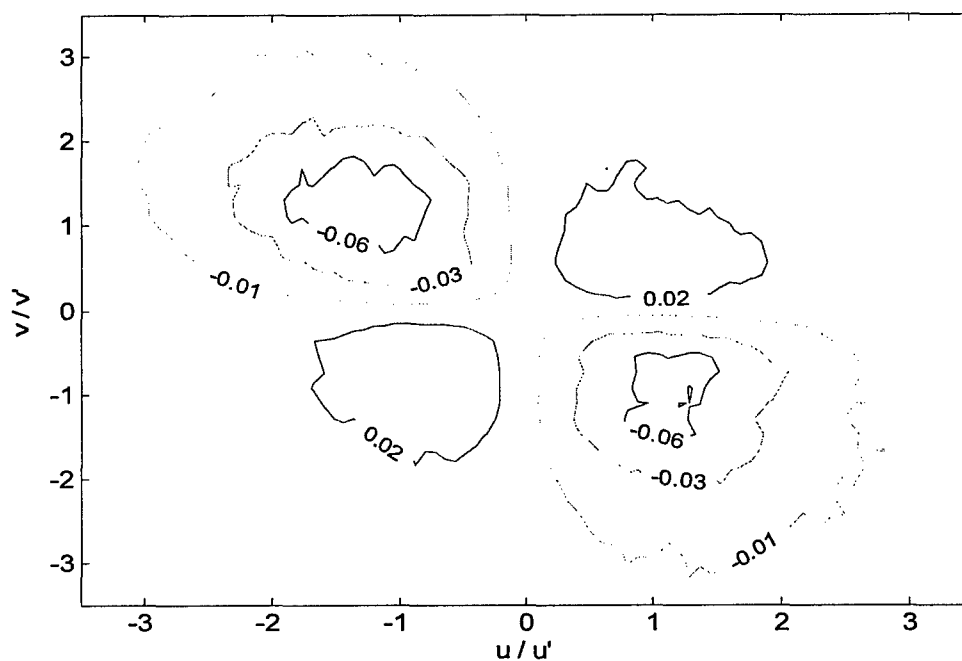


Figure 5-10 Weighted joint probability density of u and v at $y^+ = 810$.

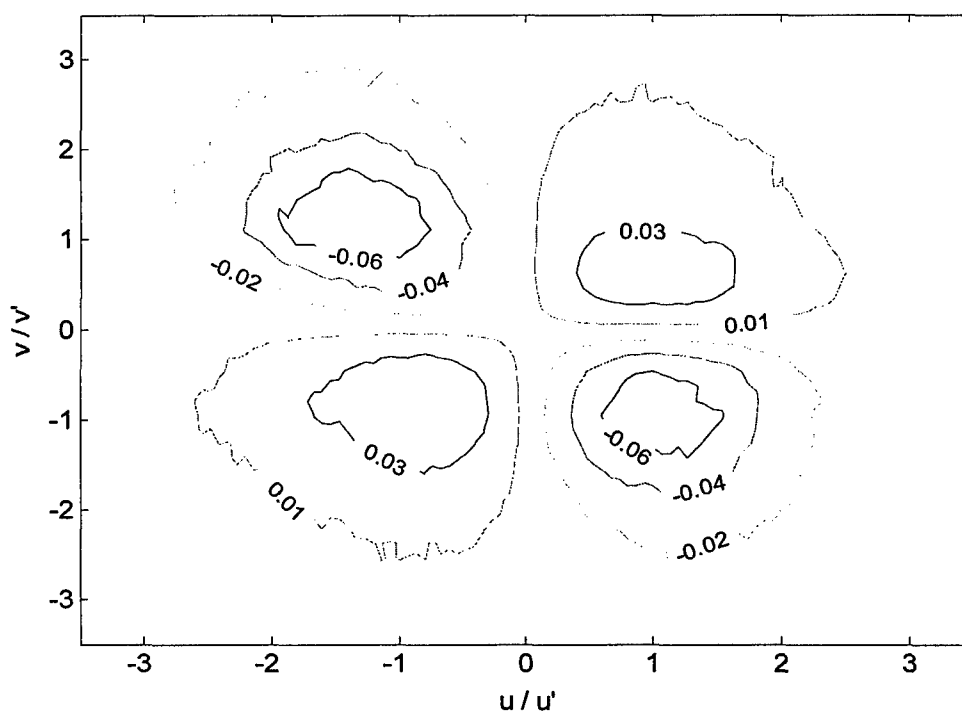


Figure 5-11 Weighted joint probability density of u and v at $y^+ = 1860$

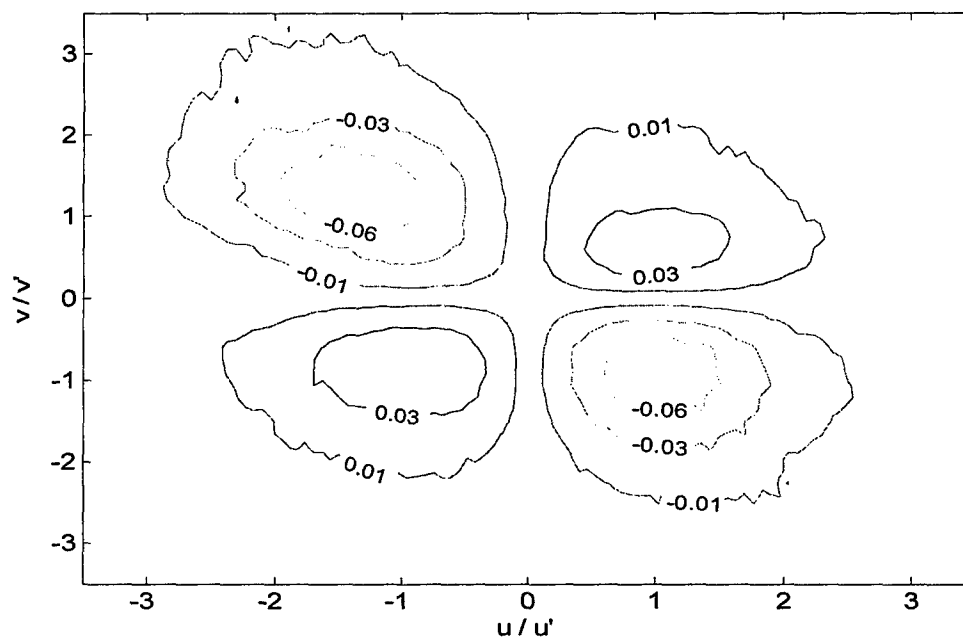


Figure 5-12 Weighted joint probability density of u and v at $y^+ = 2150$

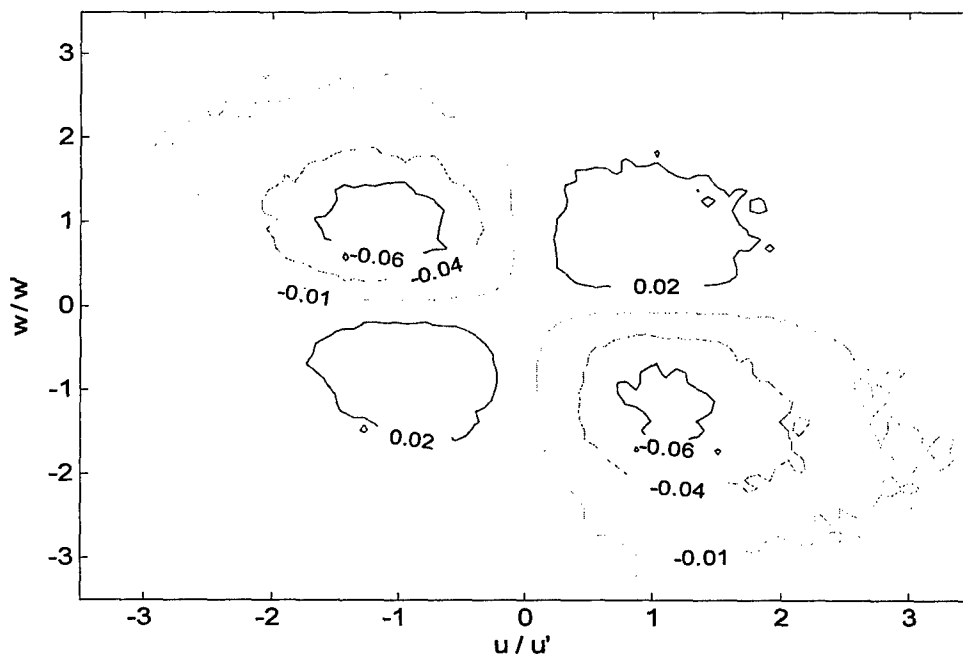


Figure 5-13 Weighted joint probability density of u and w at $y^+ = 810$

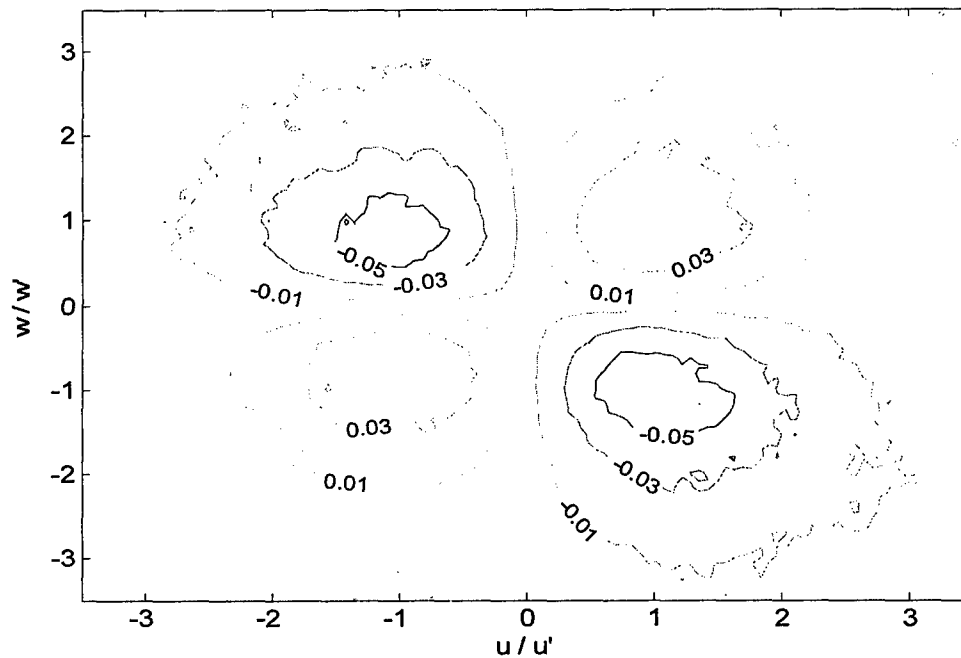


Figure 5-14 Weighted joint probability density of u and w at $y^+ = 2150$

5.2.4 Spectral Representation

Inner-normalized and premultiplied velocity autospectra are shown in figures 5-15 and 5-16. Contributions to the Reynolds stress are seen in the cospectra of u and v shown in figures 5-17 through 5-19.

As these figures show, at both $y^+ = 810$ and $y^+ = 2150$ low wavenumber contribution to v is damped in comparison to the w autospectrum, which bears a greater similarity to u in its peak. This is indicative of the near-wall measurement location, anisotropy of the turbulence, and a damping effect of v in the presence of the wall.

In comparison with u , the w spectrum does show greater spectral energy present at middle wavenumbers. Turbulent kinetic energy is believed to be generated

predominantly in u at low wavenumbers and transferred to other components and other scales. The mechanisms explaining this transfer of energy are not sufficiently understood to more fully rationalize these results. No appreciable difference is present in comparing the autospectra at $y^+ = 810$ and $y^+ = 2150$.

The uv cospectrum is of particular interest in this study. In premultiplied form, the cospectrum represents the contribution per normalized wavenumber to the mean of the product, which in this case is the kinematic Reynolds stress.

As can be seen in figures 5-17, 5-18, and 5-19 contribution to the Reynolds stress is predominately at middle wavenumbers. The location of peak contribution appears to be very near to the wave numbers which characterize the diminishing contributions to u and the increasing contributions to v . It has been postulated that turbulent structures of similar size are most able to interact with one another, this concept would be one to consider and it certainly lends itself in explaining the location of the peak in the uv cospectrum.

As with the velocity autospectra, significant differences are not present between the measurements at different y^+ .

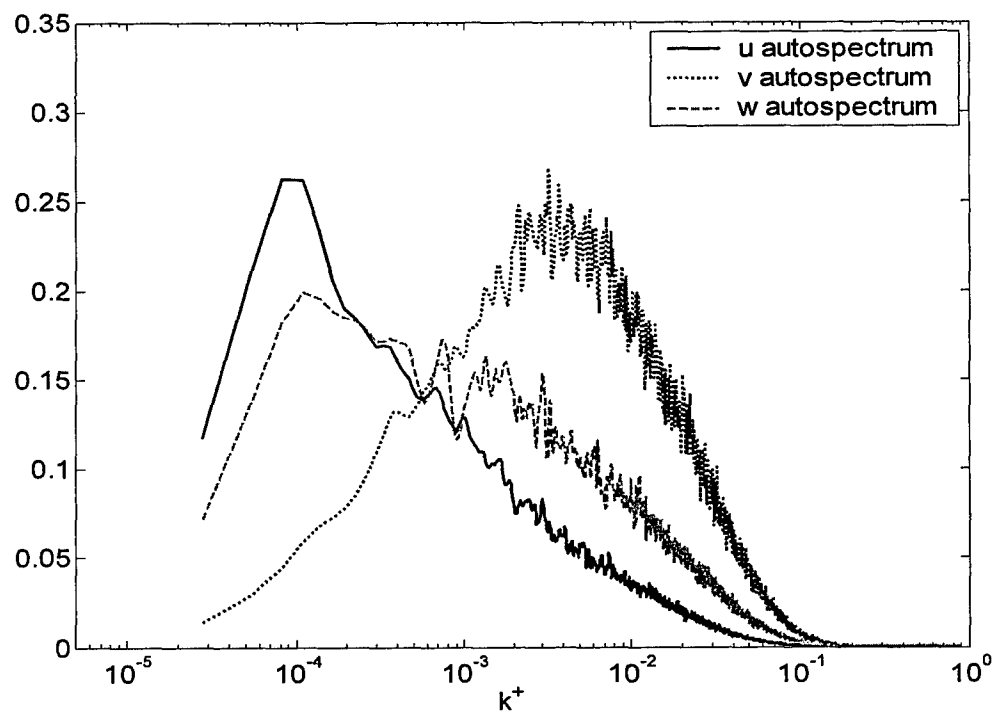


Figure 5-15 Premultiplied velocity autospectra at $y^+ = 810$

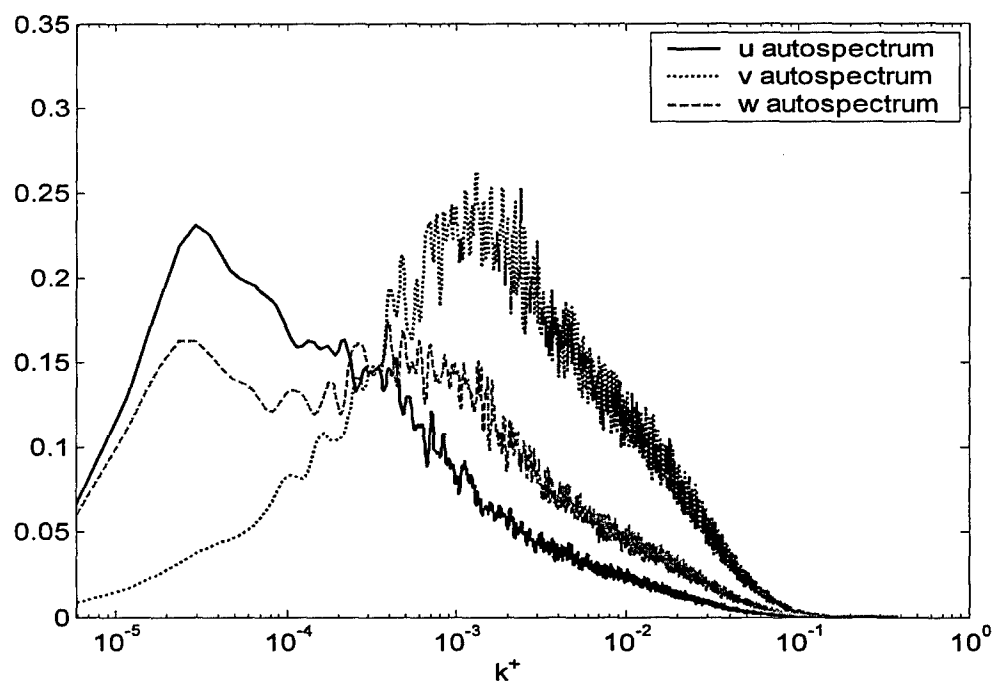


Figure 5-16 Premultiplied velocity autospectra at $y^+ = 2150$

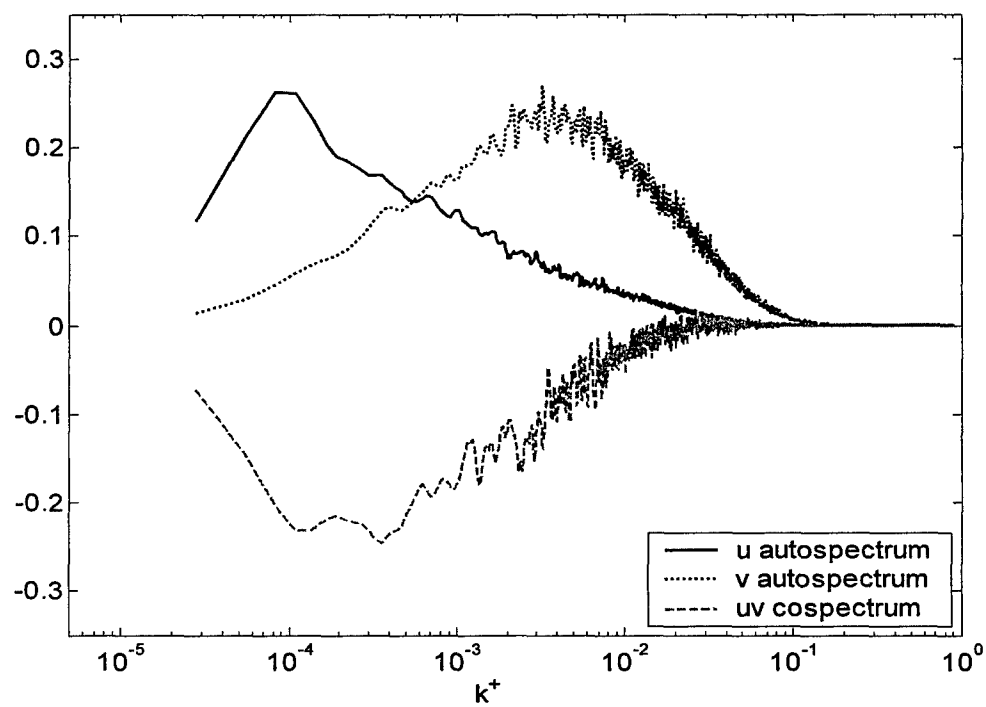


Figure 5-17 Premultiplied u and v cospectrum at $y^+ = 810$

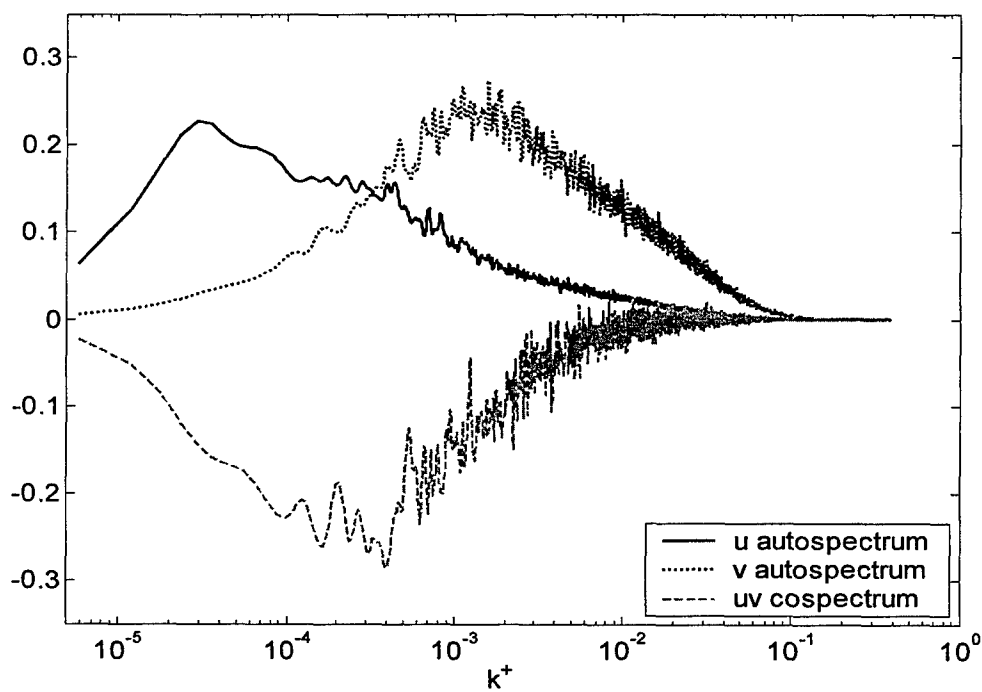


Figure 5-18 Premultiplied u and v cospectrum at $y^+ = 1860$

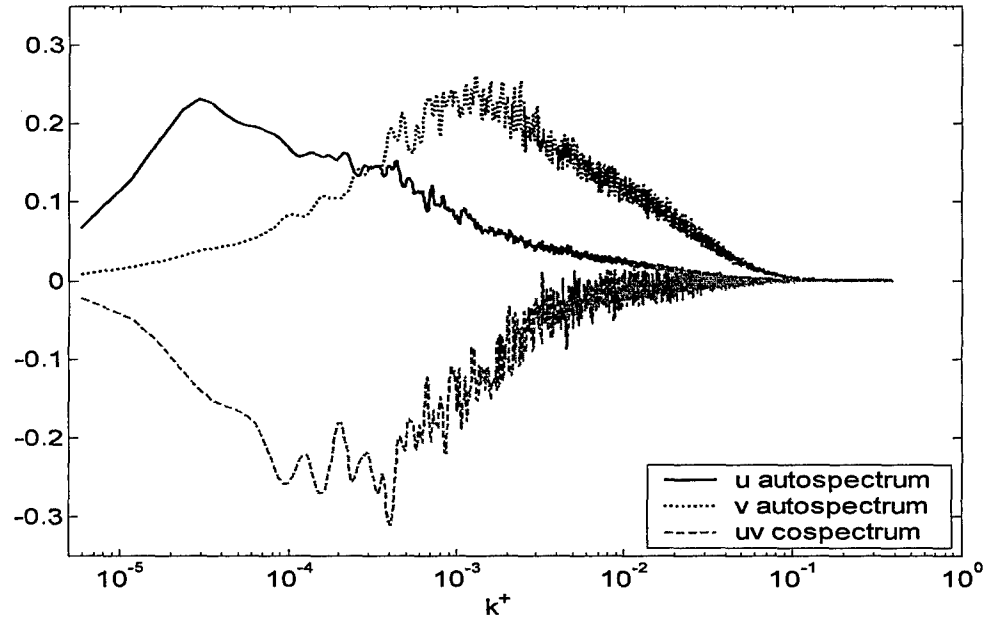


Figure 5-19 Premultiplied u and v cospectrum at $y^+ = 2150$

5.3 Vorticity and Velocity-Vorticity Statistics

5.3.1 Tabulated Results

Measured vorticity and velocity-vorticity statistical quantities are listed in dimensional form in Table 5.5. Inner-normalized values are listed in Table 5.6.

Vorticity in high Re flows is a particularly difficult quantity to measure. Although this study overcomes limitations of scale, resolution of mean velocity-vorticity products is still less than ideal. Priyadarshana *et al* (2006) plot mean velocity-vorticity products from several studies and large scatter exists between normalized values with much better agreement shown between reported fluctuation intensities. This is indicative of the difficulty in resolving accurate mean values.

The fluctuations in the velocity-vorticity product are large with respect to the mean values, and punctuated by intermittent fluctuations several standard deviations in intensity. It is clear that the mean values of the velocity-vorticity products are in a delicate balance because of their relation to the gradient of the kinematic Reynolds shear stress, which must be a small quantity. Using present techniques, there is insufficient resolution to use the means of the velocity-vorticity products as a reliable measure of the gradient of the Reynolds stress.

Table 5-5 Vorticity Statistics

Vorticity Statistics	y+ = 810	y+ = 1860	y+ = 2150	units
ω_z'	62	174	124	s^{-1}
ω_y'	20	n/a	76	s^{-1}
$\overline{v\omega_z}$	-0.9	-6.3	-8.0	m/s^2
$\overline{w\omega_y}$	-2.1	n/a	2.2	m/s^2
$\overline{u\omega_z}$	2.45	8.7	6.0	m/s^2
$(v\omega_z)'$	7.6	60.6	49.2	m/s^2
$(w\omega_y)'$	6.5	n/a	47.7	m/s^2
$(u\omega_z)'$	18.6	157	115.1	m/s^2
$\overline{w\omega_y - v\omega_z}$	-1.2	n/a	-10.2	m/s^2
Mean Event Duration ω_z	0.0145	0.0014	0.0019	s
Mean Event Duration ω_y	0.0053	n/a	0.0007	s
$v\omega_z$ correlation coeff.	-0.14	-0.11	-0.21	
$w\omega_y$ correlation coeff.	-0.62	n/a	0.06	
$u\omega_z$ correlation coeff.	0.17	0.07	0.06	
$u\omega_y$ correlation coeff.	0.56	n/a	-0.01	

Table 5-6 Inner Normalized Vorticity Statistics

Vorticity Statistics	y+ = 810	y+ = 1860	y+ = 2150
$\omega_z'^+$	0.115	0.046	0.033
$\omega_y'^+$	0.037	n/a	0.020
$\overline{v\omega_z}^+$	-0.017	-0.006	-0.008
$\overline{w\omega_y}^+$	-0.040	n/a	0.002
$\overline{u\omega_z}^+$	0.045	0.009	0.006
$(v\omega_z)'^+$	0.140	0.060	0.049
$(w\omega_y)'^+$	0.120	n/a	0.047
$(u\omega_z)'^+$	0.34	0.157	0.115
$\overline{w\omega_y - v\omega_z}^+$	-0.023	n/a	-0.006
Mean Event Duration ω_z	7.84	5.31	7.21
Mean Event Duration ω_y	2.86	n/a	2.66

5.3.2 Probability Density

A negative velocity-vorticity correlation is observed in $v\omega_z$ at each value of y^+ . The weighted joint probability distribution reveals a strong $v\omega_z$ weighting in quadrant four at $y^+=810$, whereas at $y^+ = 2150$ the $v\omega_z$ weighting is strongest in quadrant two.

A difference is observed in the sign of the correlation in $w\omega_y$ between $y^+ = 810$ and $y^+ = 2150$. At $y^+ = 2150$ the $w\omega_y$ correlation is positive whereas at $y^+ = 810$ the correlation is very distinctly negative.

At y_p the gradient of the Reynolds stress is zero. It follows that both the $w\omega_y$ and $v\omega_z$ correlations should be of the same sign if they are to subtract to zero. This, however, was not observed. As previously noted, y_p approximately varies with the square-root of l^+ , however boundary layer thickness was not precisely determined on these dates.

At y^+ values lower than y_p a negative gradient should be seen in $\partial \overline{uv} / \partial y$. At $y^+ = 810$, $\overline{w\omega_y}$ and $\overline{v\omega_z}$ were found to be of the same sign (negative) and $\overline{v\omega_z}$ smaller in magnitude which might suggest $y^+ < y_p$.

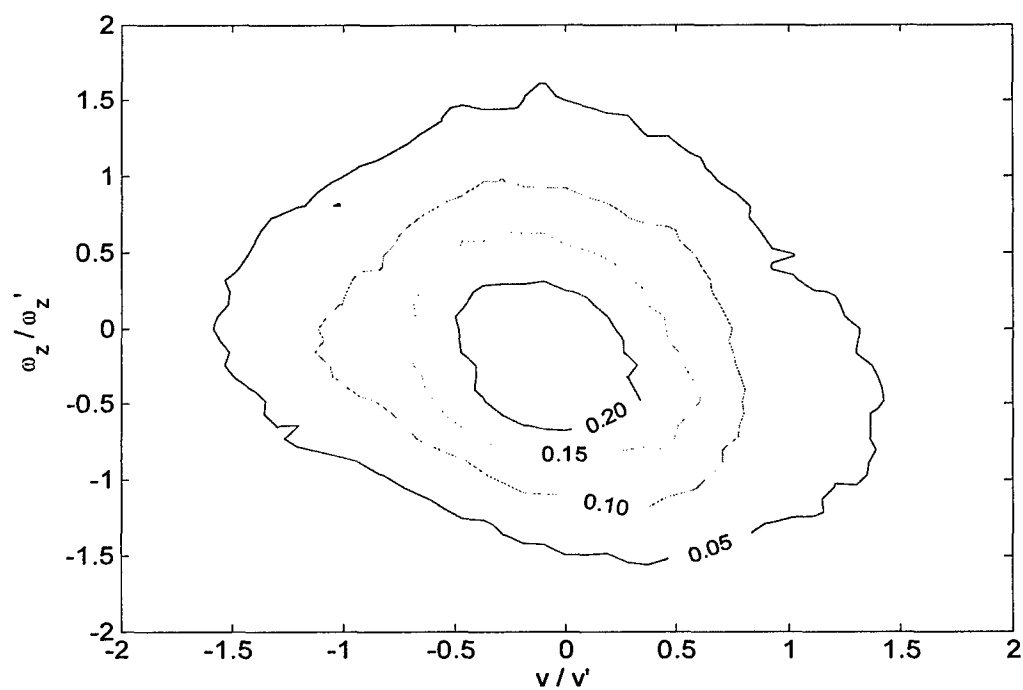


Figure 5-20 Joint probability density of v and ω_z at $y+ = 810$

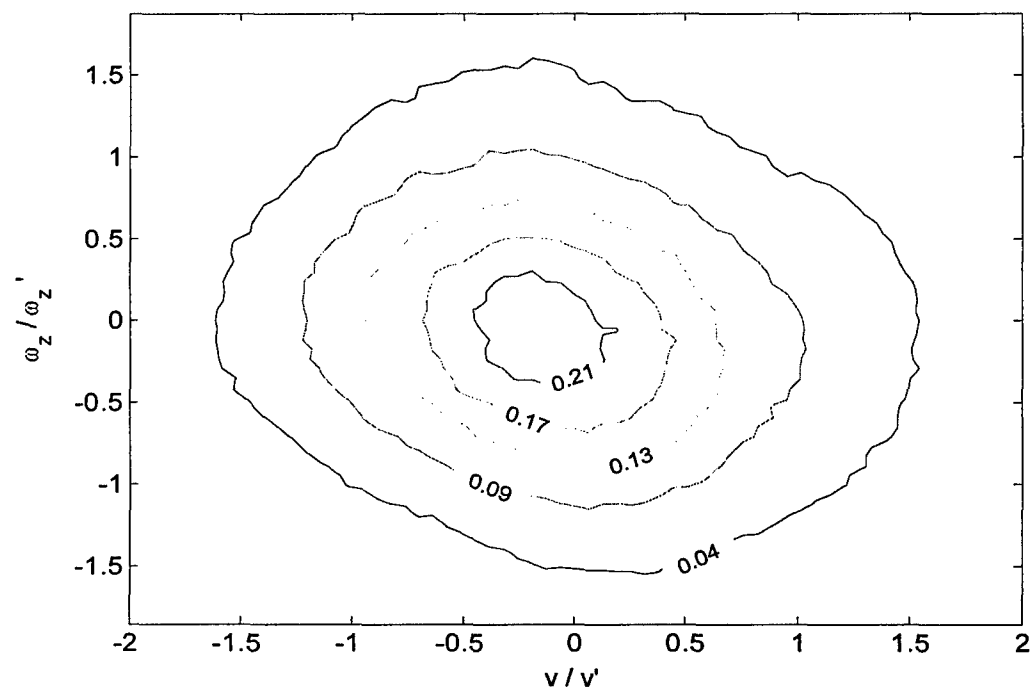


Figure 5-21 Joint probability density of v and ω_z at $y+ = 1860$

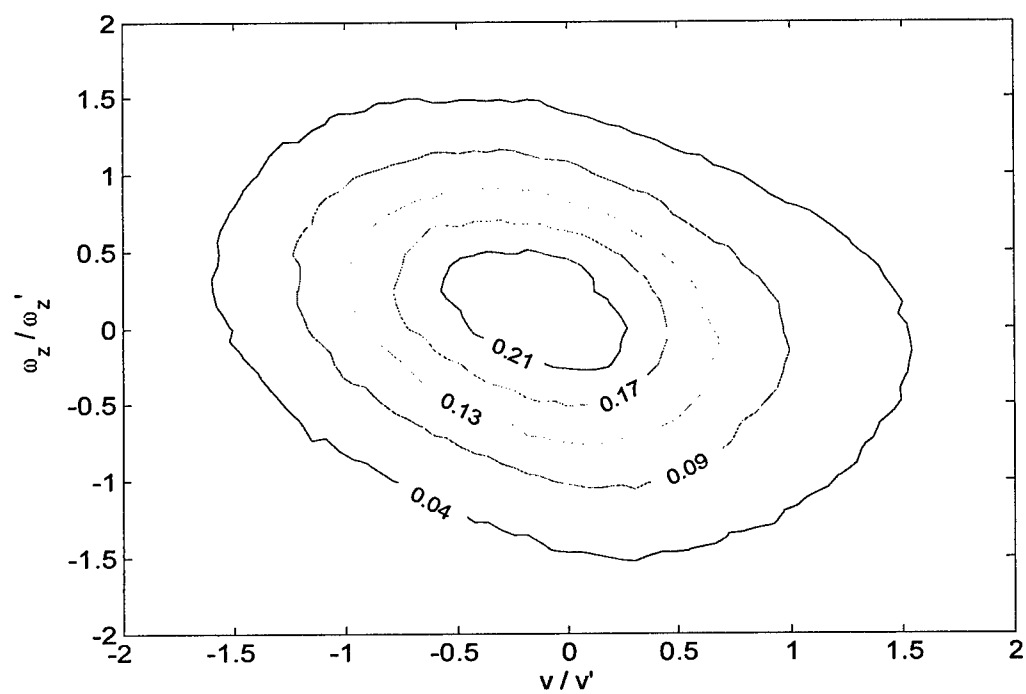


Figure 5-22 Joint probability density of v and ω_z at $y^+ = 2150$

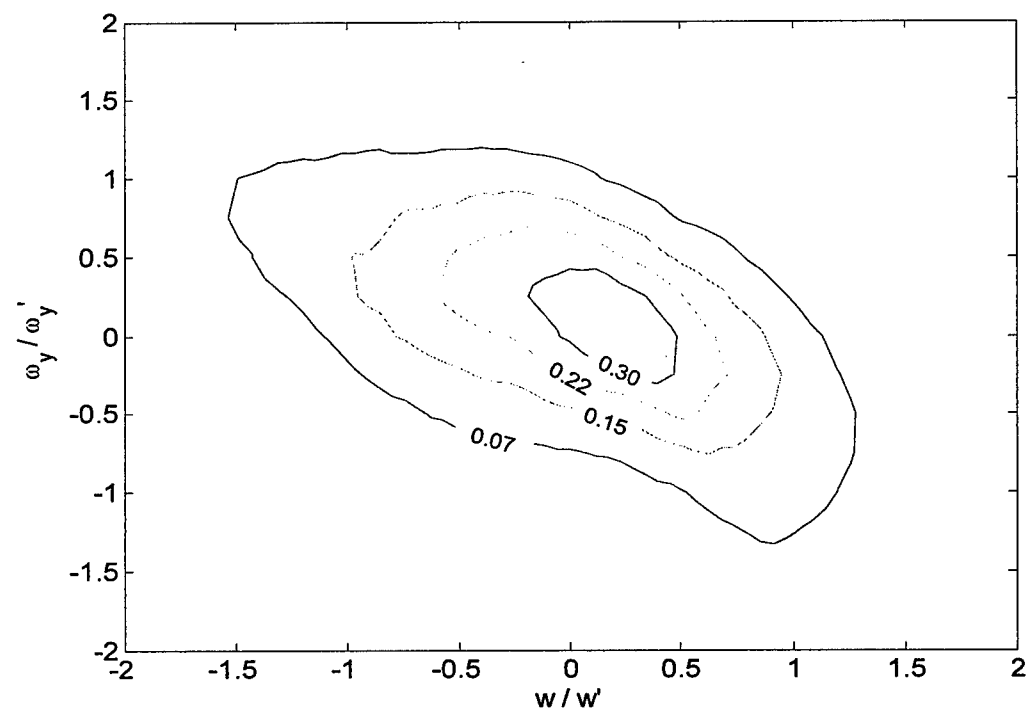


Figure 5-23 Joint probability density of w and ω_y at $y^+ = 810$

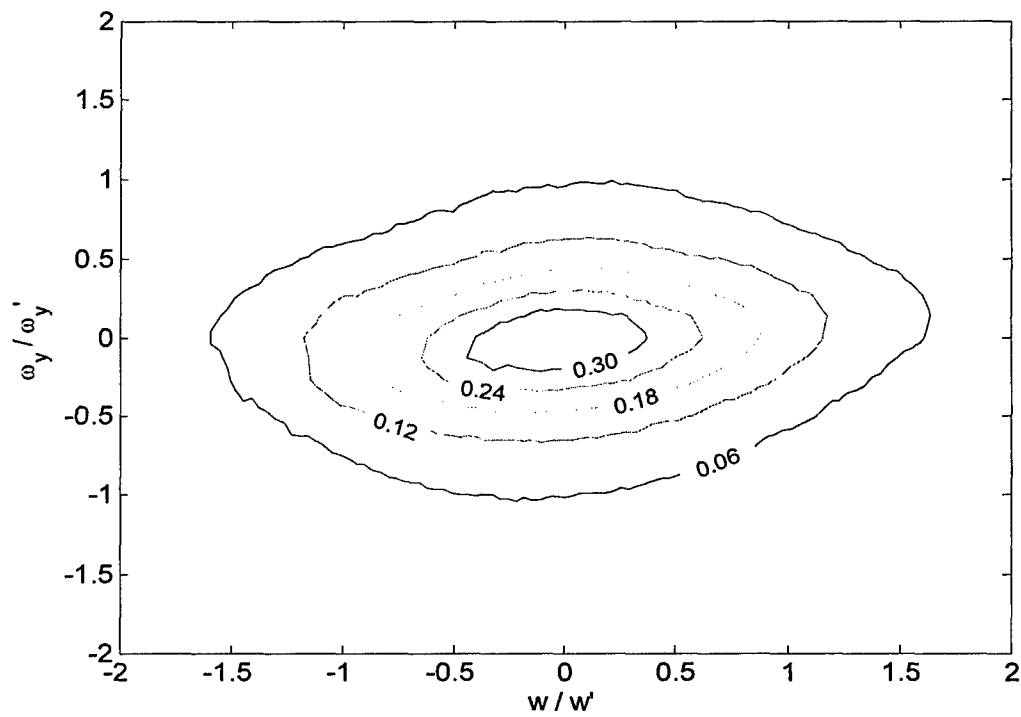


Figure 5-24 Joint probability density of w and ω_y at $y^+ = 2150$

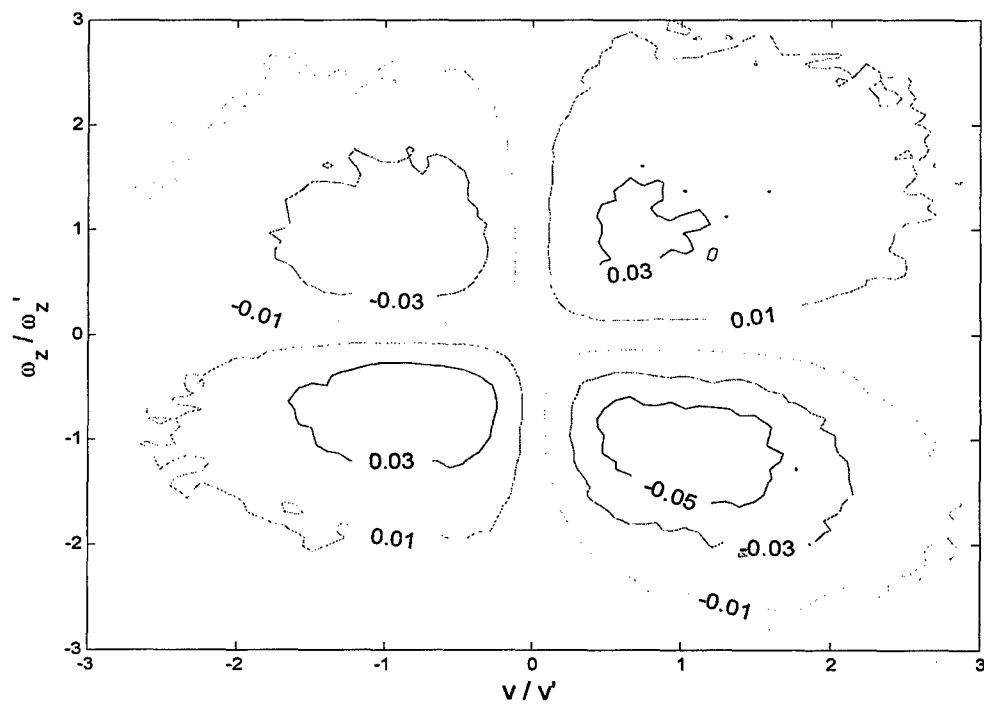


Figure 5-25 Weighted joint probability density of v and ω_z at $y^+ = 810$

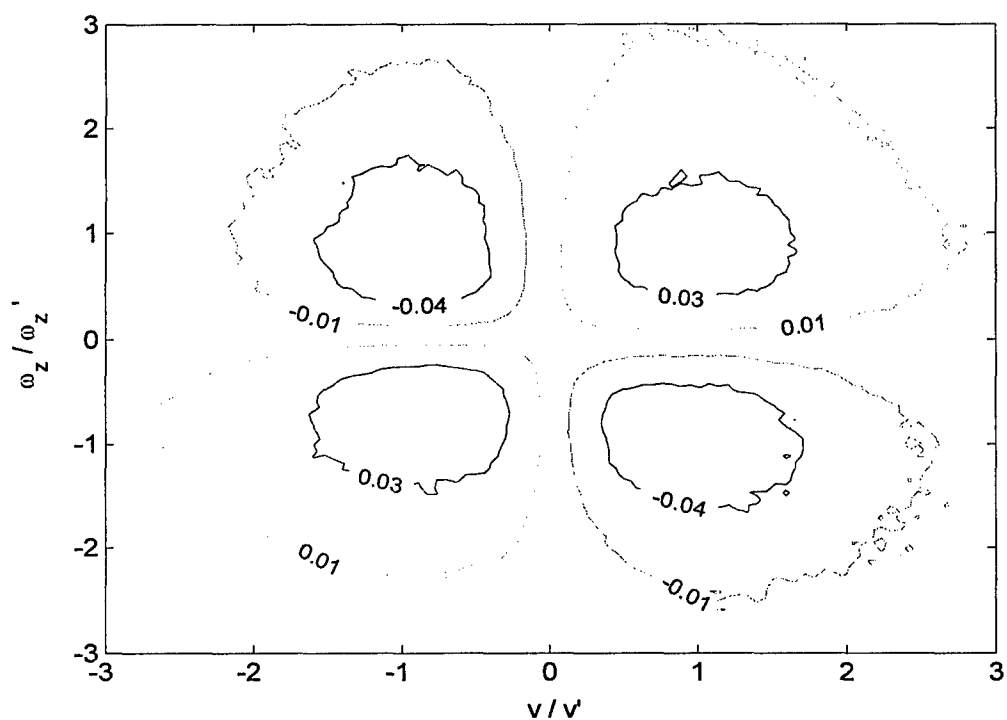


Figure 5-26 Weighted joint probability density of v and ω_z at $y^+ = 1860$

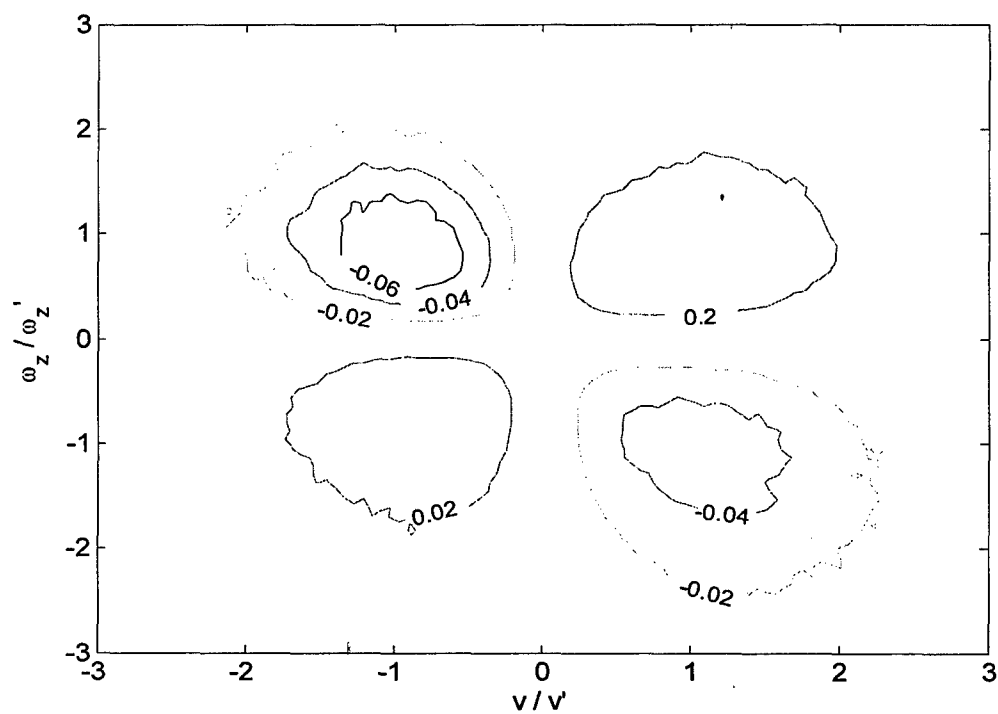


Figure 5-27 Weighted joint probability density of v and ω_z at $y^+ = 2150$

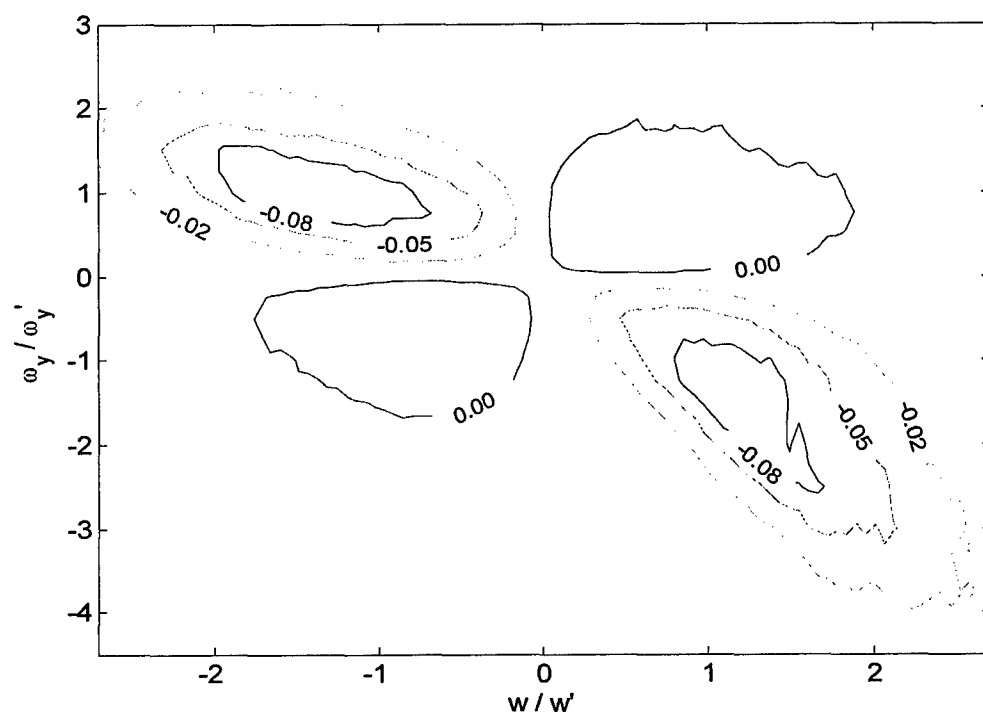


Figure 5-28 Weighted joint probability density of w and ω_y at $y^+ = 810$

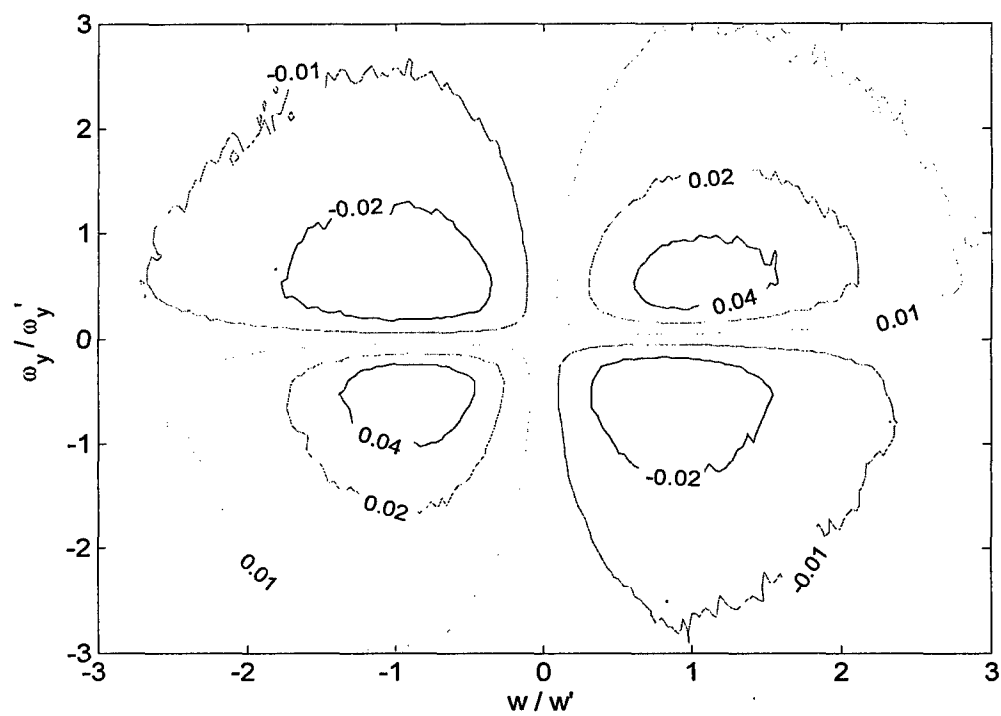


Figure 5-29 Weighted joint probability density of w and ω_y at $y^+ = 2150$

5.3.3 Spectral Representation

Normalized and premultiplied vorticity autospectra are presented in figures 5-30 and 5-31. Velocity-vorticity autospectra are compared with velocity-vorticity cospectra in figures 5-32 and 5-38.

While the mean values of velocity-vorticity products are difficult to resolve, the fluctuating components are large. The spectral representation of velocity, vorticity, and velocity-vorticity products provides insight into the interaction and contribution at different wavenumbers to the important products representative of the gradient of the kinematic Reynolds shear stress.

A key result of the vorticity autospectra is the emergence of a high-wavenumber peak. At $y^+ = 810$ the peak in the ω_z autospectrum occurs at relatively low-wavenumber and only a slight "bulge" is present at higher wavenumbers. The ω_y autospectrum at $y^+ = 810$ has one peak at low wavenumbers and a distinct second peak at high wavenumbers is also present.

In comparison, at $y^+ = 2150$ both the ω_z and ω_y autospectra have distinct peaks at high-wavenumbers with the ω_y peak again more prominent than that for ω_z .

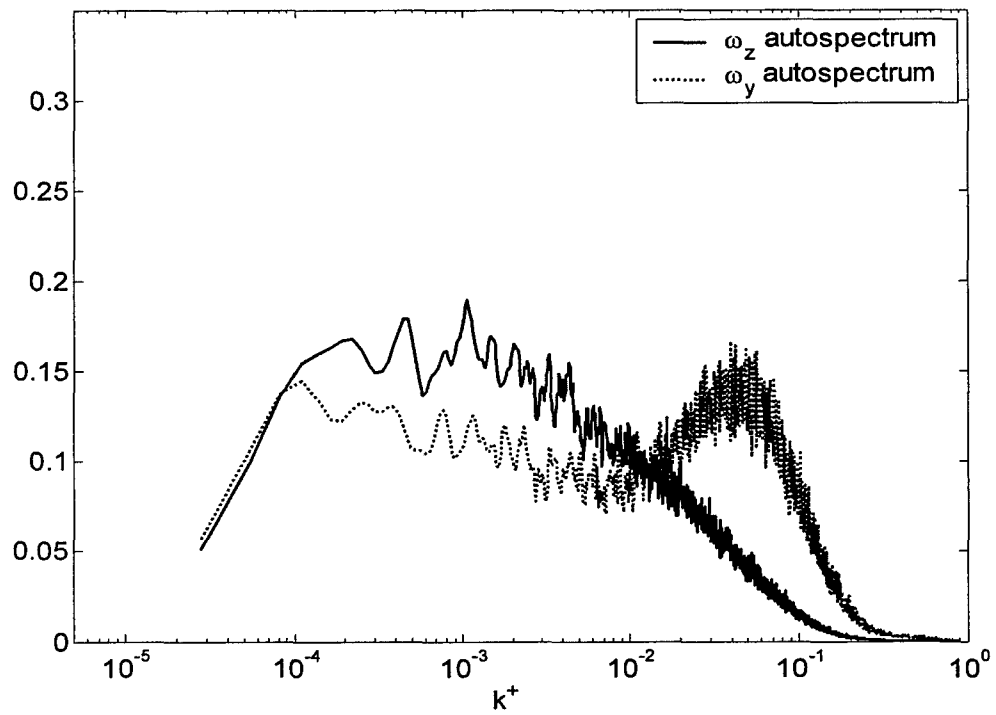


Figure 5-30 Premultiplied ω_z and ω_y autospectra at $y^+ = 810$

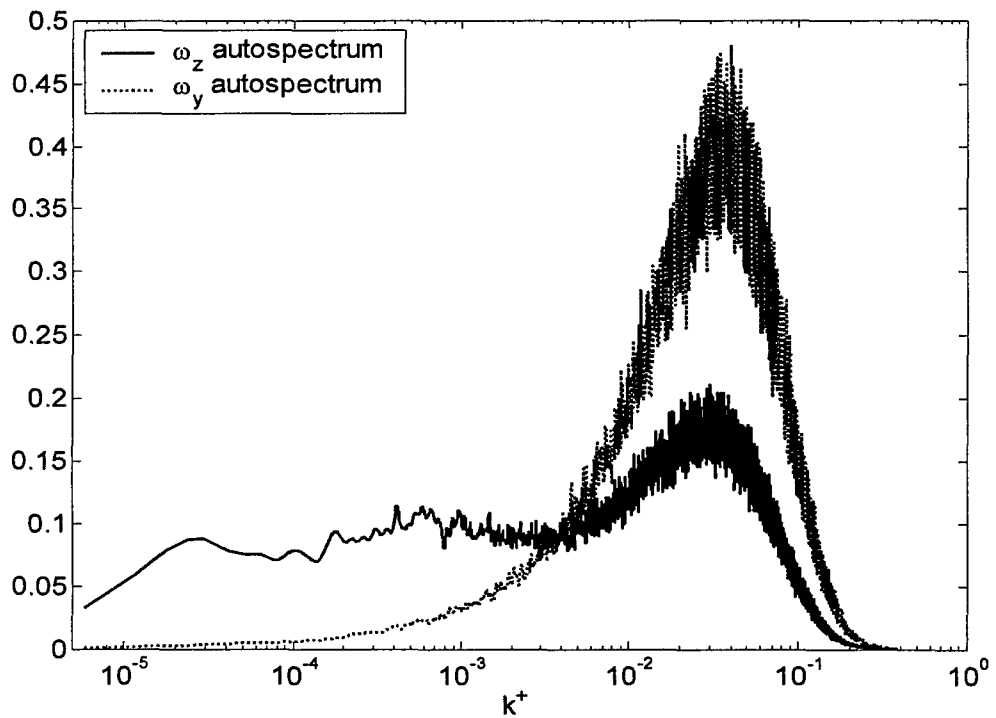


Figure 5-31 Premultiplied ω_z and ω_y autospectra at $y^+ = 2150$

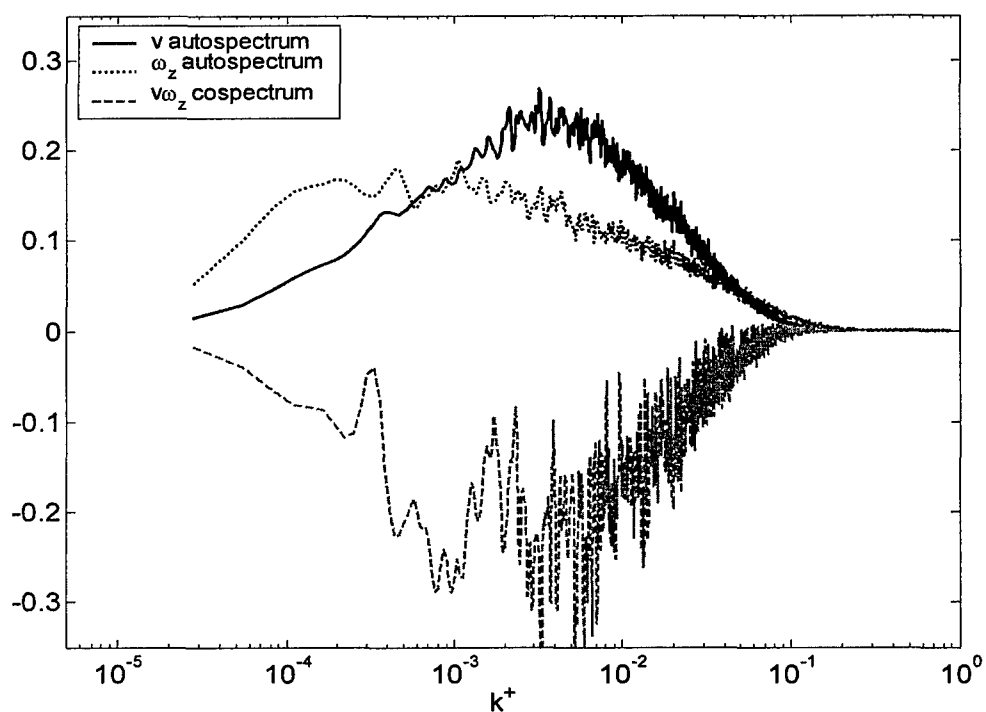


Figure 5-32 Premultiplied v and ω_z cospectrum at $y^+ = 810$

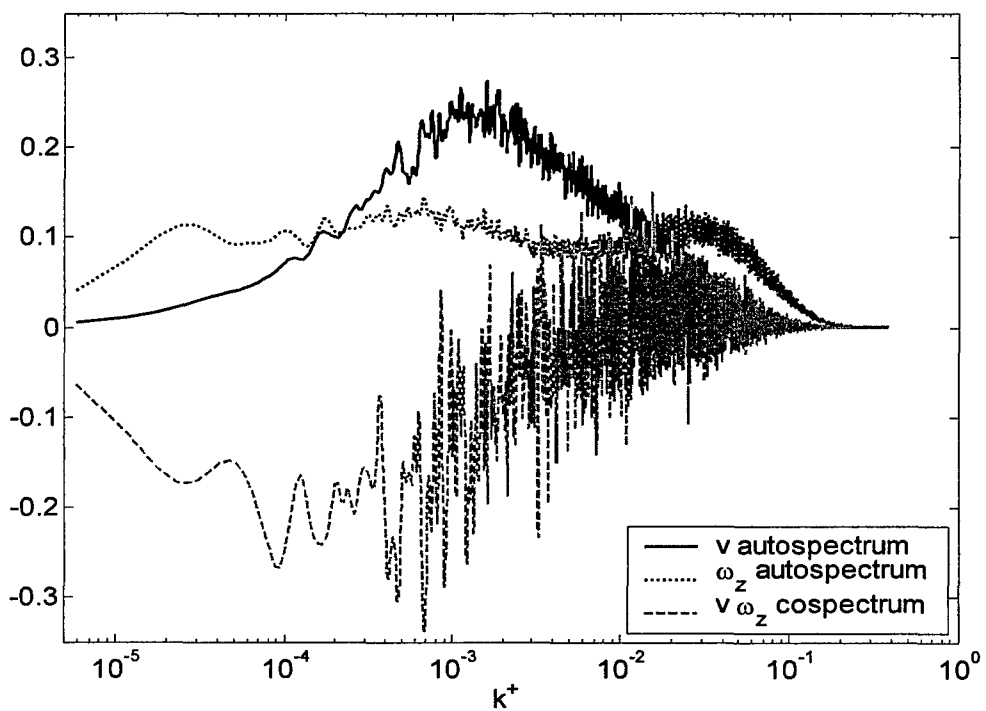


Figure 5-33 Premultiplied v and ω_z cospectrum at $y^+ = 1860$

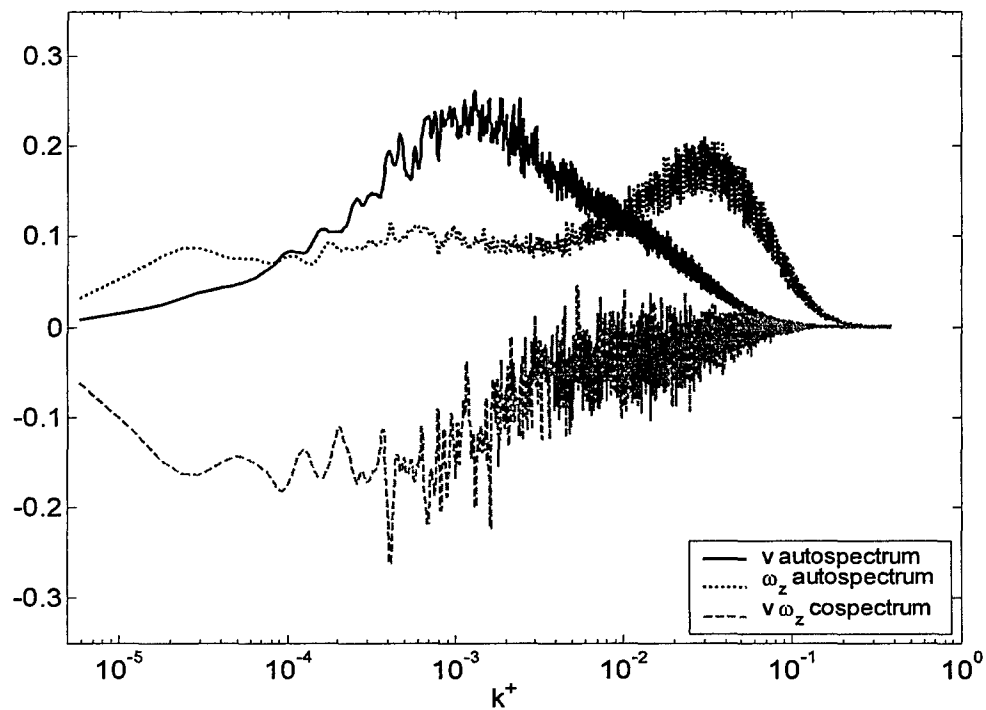


Figure 5-34 Premultiplied v and ω_z cospectrum at $y^+ = 2150$

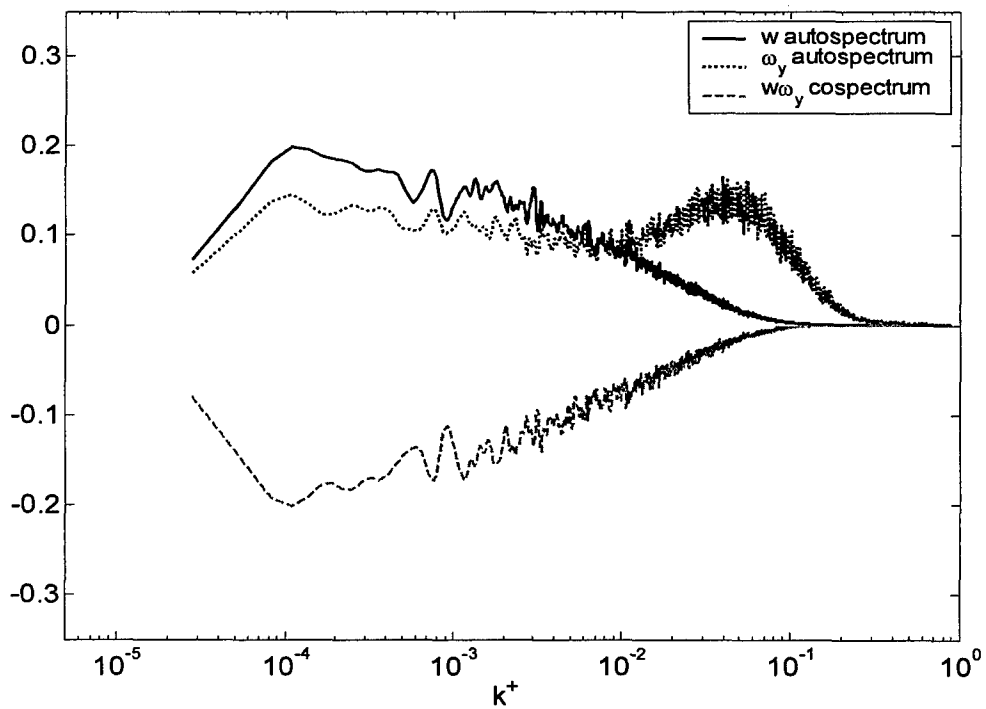


Figure 5-35 Premultiplied w and ω_y cospectrum at $y^+ = 810$

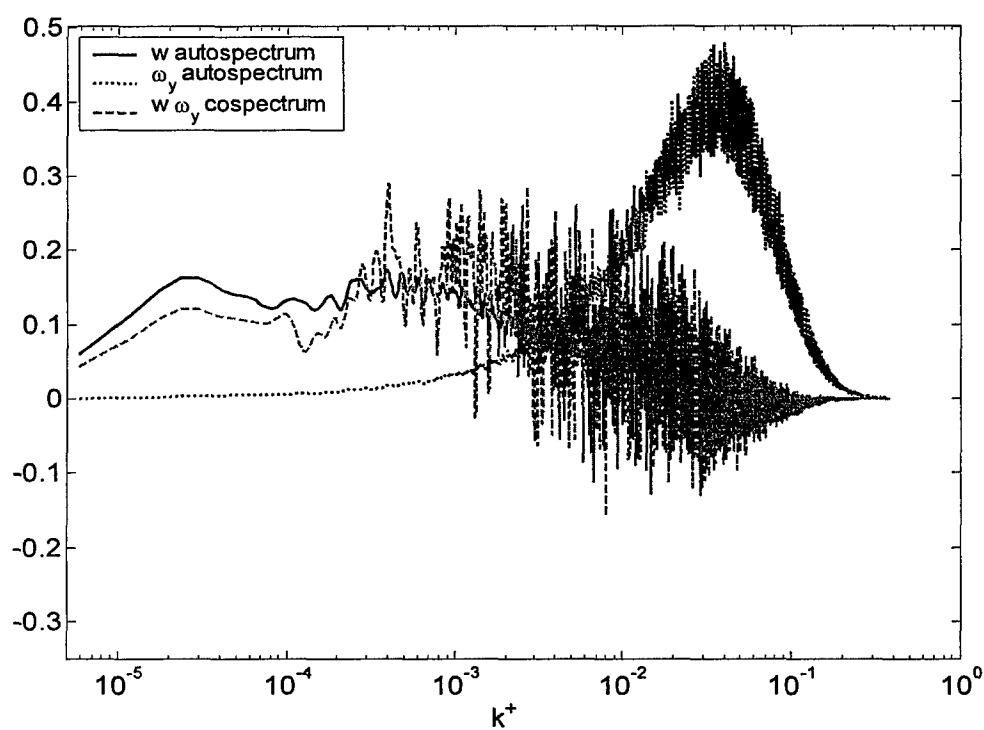


Figure 5-36 Premultiplied w and ω_y cospectrum at $y^+ = 2150$

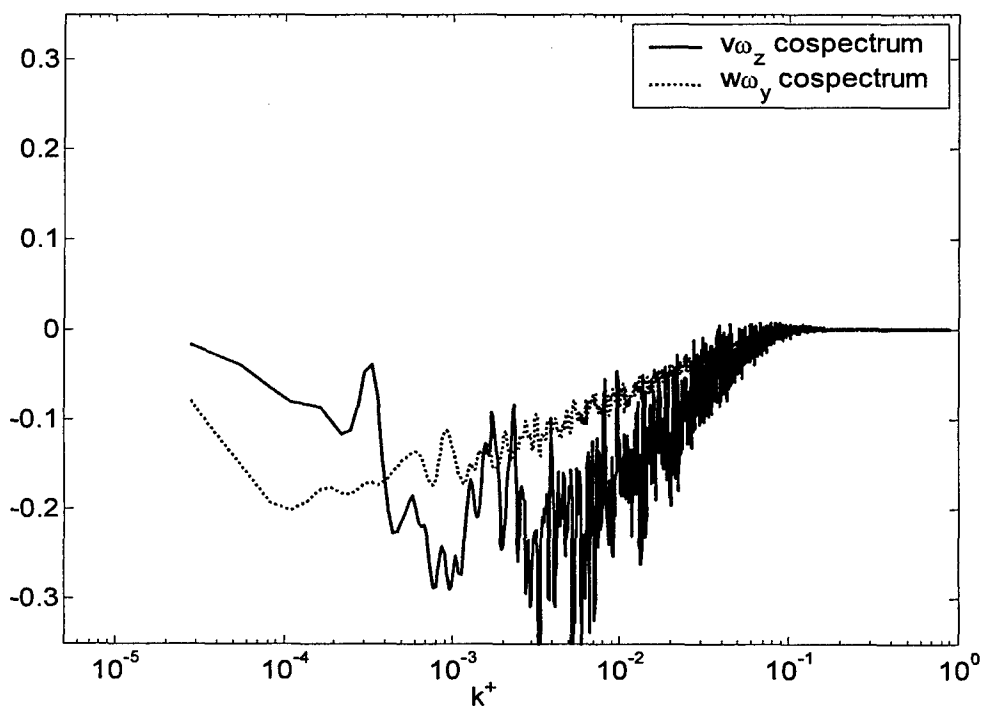


Figure 5-37 Premultiplied $v\omega_z$ and $w\omega_y$ cospectra at $y^+ = 810$

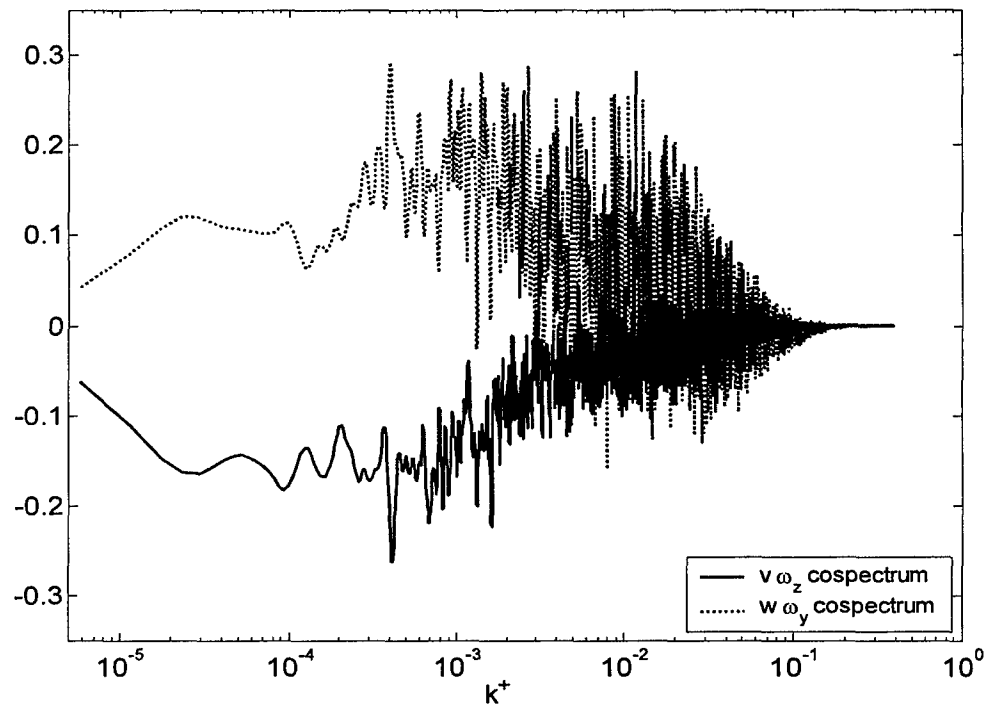


Figure 5-38 Premultiplied $v\omega_z$ and $w\omega_y$ cospectra at $y^+ = 2150$

6. Conclusions

Velocity and vorticity measurements in the atmospheric surface layer were collected on two evenings under nearly neutral conditions at the SLTEST site, Dugway, Utah. The following conclusions are supported by these measurements.

- Statistical data for the mean velocity (U), the u, v, w and the vorticity component fluctuations have been provided in dimensional and inner-normalized form. It is expected that these data will be of particular interest to those engaged in CFD efforts to characterize very high R_θ turbulent boundary layers.
- Probability density functions of the velocity components reveal that a large fraction of the fluctuating intensities are uncorrelated.

- The cospectra for u,v exhibits a distinct peak for the wave numbers at which the u contribution is falling whereas the v contribution is rising. This pattern is particularly distinct for the larger y^+ values.
- The velocity-vorticity statistics clarify that the desired balance, that would produce the $-\overline{\partial uv}/\partial y$ value, is too subtle an attribute of the widely distributed $v\omega_z$ and the $w\omega_y$ products. This inference is supported by the joint pdf's. It is instructive to note the rich populations of fluctuations. It is also instructive that the $w\omega_y$ correlation is more "well defined" than the $v\omega_z$ correlation.
- At $y^+ = 1860$ and $y^+ = 2150$ both ω_z and ω_y autospectra have peaks at relatively high wavenumbers, whereas at $y^+ = 810$ ω_z no such high wavenumber peak is present. The peak is more prominent in ω_y than in ω_z at both values of y^+ .
- The cospectra of velocity and vorticity indicate that contributions to the gradient of the kinematic Reynolds stress by both $v\omega_z$ and $w\omega_y$ occur primarily at intermediate and lower wavenumbers.

REFERENCES

Andreopoulos, J., and Honkan, A. 2001 "An experimental study of the dissipative and vortical motion in turbulent boundary layers." *J. Fluid Mech.* 439, 131-163.

Balint, J., Wallace, J.M. & Vukoslavcevic, P. 1991 "The velocity and vorticity vector fields of a turbulent boundary layer. Part 2. Statistical properties." *J. Fluid Mech.* 228, 53-86.

DeGraaff, D.B., and Eaton, J.K. 2000 "Reynolds-number scaling of the flat-plate turbulent boundary layer." *J. Fluid Mech.* 422, 319-346.

Honkan, A., Andreopoulos Y. 1997 "Vorticity, strain-rate and dissipation characteristics in the near-wall region of turbulent boundary layers." *J. Fluid Mech.* 350, 29-96.

Klewicki, J.C. 1989 "Velocity-vorticity correlations related to the gradients of the Reynolds stress in parallel turbulent wall flows." *Phys. Fluids* Vol 1 No. 7, 1285-1288

Maher, M. 2002 "Velocity and vorticity measurements in the atmospheric boundary layer." Master Thesis, Michigan State University, East Lansing, MI.

Metzger, M.M. & Klewicki, J.C. 2000 "A comparative study of near-wall turbulence in high and low Reynolds number boundary layers." *Physics of Fluids* Vol. 13 Issue 3, 692-701.

Metzger, M.M., Klewicki, J.C., Bradshaw, K.L., and Sadr R. 2001 "Scaling the near-wall axial turbulent stress in the zero pressure gradient boundary layer." *Physics of Fluids* Vol. 13 Issue 6, 1819-1821.

Ong, L. and Wallace, J.M. 1998 "Joint probability density analysis of the structure and dynamics of the vorticity field of a turbulent boundary layer." *J. Fluid Mech.* 367, 291-328.

Priyadarshana, P. 2004 "Reynolds number influences on turbulent boundary layer momentum transport." Doctoral thesis, The University of Utah, Salt Lake City, UT.

Priyadarshana, P.A., Klewicki, J.C., Treat, S. & Foss, J.F. "Experimental study of turbulent boundary layer velocity-vorticity products at high and low Reynolds numbers." (2006 Approved for publication in Journal of Fluid Mechanics.)

Priyadarshana, P.A., Paththage, Klewicki, J.C., Treat, S. and Foss, J. F.(2006) "Statistical structure of turbulent boundary layer velocity-vorticity products at high and low Reynolds numbers," accepted for publication, Jour. Fl. Mech.(JFM-05-S-0500.R1).

Surface Layer Turbulence and Environmental Test Facility home page.
<http://www.mech.utah.edu/sltest/>

Wallace, J.M. and Foss, J.F. 1995 "The measurement of vorticity in turbulent flows." *Annu. Rev. Fluid Mech.* 27, 469-514.

Wei, T., Klewicki, J., and McMurtry, P. 2003 "Scaling properties of the mean momentum balance in turbulent wall layers." *J. Fluid Mech.*

Krogstad, P.A., Antonia, R.A., and Browne W.B. 1992 "Comparison between rough- and smooth-wall turbulent boundary layers." *J. Fluid Mech.* 245, 599-617.

Foss, J.F., Bohl, D.G., and Hicks, T.J. 1996 "The pulse width modulated-constant temperature anemometer" *Meas. Sci. Technol.* 7, 1388-1395.

Sreenivasan, K.R., Gad el Hak, E. 1989 "The turbulent boundary layer" *Frontiers in Experimental Fluid Mechanics* 159-209.

Foss, J.F., and Hicks, T.J. 2001 "Processing time series data (velocity, shear stress) from the pulse width modulated-constant temperature anemometer (PWM-CTA) *Unknown Journal Unknown Volume*, 448-456.

Pope, Stephen NB. Turbulent Flows. Cambridge University Press, United Kingdom, 2000.

Morris, S.C., "The Velocity and Vorticity Fields of a Single Stream Shear Layer." Ph.D. dissertation, Michigan State University, East Lansing, MI 2002.

Bernard, P. and Wallace J. Turbulent Flow. John Wiley & Sons, 2002.

Tennekes, H. and Lumley, J.L. A First Class in Turbulence. The MIT Press, 1972.

Klewicki, J.C., Priyadarshana, P., Foss, J.F., and Sreenivasan, K.R., "Boundary Layer Turbulence Measurements at Submarine Scale Reynolds Numbers to Support RANS Model Validation and Development." First Year Progress Report, ONR, 1992.